BROADBAND MEASUREMENTS OF THE ACOUSTIC BACKSCATTER CROSS SECTION OF SAND PARTICLES IN SUSPENSION

CHENG HE

BROADBAND MEASUREMENTS OF THE ACOUSTIC BACKSCATTER CROSS SECTION OF SAND PARTICLES IN SUSPENSION

by

Cheng He

A Thesis submitted to the School of Graduate Studies in partial fulfillment of the requirements for the degree of Master of Science

Department of Physics
Memorial University of Newfoundland
October, 1991

St. John's Newfoundland

ISBN 0-315-73290-3

ABSTRACT

A method using a broadband acoustic transducer to measure the acoustic backscatter cross section of suspended particles in the nearfield of the transducer is investigated. In order to understand the behaviour of acoustical pressure in the nearfield, a closed-form expression for the acoustical field produced by a circular piston with simply supported boundary condition is derived, extending the earlier work of Hasegawa et al. (1983,1984) to include the case of non-uniform velocity at the piston surface. The average pressure on the surface of the receiver as a function of distance from the transmitter is calculated theoretically and measured experimentally. The measured results at the centre frequency of the transmitter/ receiver pair are in reasonable agreement with the theoretical calculation, although the change of the average pressure with distance in the nearfield is larger for all frequencies than previously thought. However, it should still be possible to measure a uniform distribution of particles suspended in the nearfield. Beginning with backscattering from a movable rigid sphere, a nearfield expression relating the output of the receiver to the concentration and average size of suspended particles and to the backscatter form factor, $f_\infty(x)$, is obtained. The form factor is determined by measuring the backscattered radiation from suspended natural

sand of known concentration and size. The frequencies used for measurement range from 1.3 MHz to 2.8 MHz, and the sand sizes from 100 to 500 μm diameter. The measured form factor follows the theoretical expression calculated from the movable rigid sphere model reasonably well, although as the product of particle radius and source wavenumber increases, the measured values are larger than predicted by the spherical scatterer model. This is similar to measurements made previously with narrowband systems, and is probably due to the irregular shapes and inhomogenous composition of natural sand grains. The research as a whole shows that though the acoustical nearfield is much more complex than the farfield, scattering cross section measurements can be made in the nearfield, with broadband pulses, at high resolution in frequency.

ACKNOWLEDGEMENTS

The author wishes to thank the Department of Physics for affording him the opportunity of conducting this work. Particularly, the supervision of Dr. Alex Hay and his suggestion of an exciting research topic in the author's field of interest are greatly appreciated.

Dr. A. Hay, Dr. R. J. Greatbatch, Dr. B. Sanderson, and Dr. B. de Young are to be especially thanked for insight provided in courses relating to this work. Members of the Oceanography Group at the Department of Physics, in particular Dr. J. Sheng, Mr. D. Wilson, Mr. A. Goulding, Mr. C. Hamm, Ms. A. Crawford, Mr. R. Campbell and H. Halide, have also provided valuable assistance at various stages of this work.

I am deeply appreciative of the finacial assistance from Memorial University of Newfoundland in the form of a University Fellowship, Teaching Assistantship, and Dr. Hay's grants from the Department of Energy, Mines, and Resources, and the Natural Sciences and Engineering Research Council of Canada.

Finally, the patience and understanding of the author's wife during the research period is deeply appreciated.

Contents

List of Figures

List of Tables

Chapter 1

INTRODUCTION

1.1 Statement of the Problem

The importance of grain size and concentration estimation acoustically has long been recognized in examining movement of sediment (Flammer,1962), coal slurry transport (Davis,1978) and cells in the blood stream (Siegelmann and Reid, 1973). During the past few decades, many new optical and acoustical measurement methods and apparatus have been proposed and built according to the principle that a wave will be scattered by the suspended particles. A problem with the optical method in aqueous suspensions is that the wave decays very rapidly. Also, the optical wavelengths used

are usually very short compared to the particle size. Thus it is difficult for optical methods to detect suspended particles remotely, and these methods are mainly confined to measurement of fine sediment in suspension.

The ultrasonic pulse-echo technique has been proven to be a simple and efficient method for measurement of particles suspended in water (Flammer 1962; Greenlaw and Johnson, 1982; Holliday, 1987; Hay 1991; Sheng and Hay, 1991). The central problem in acoustical scattering techniques lies in determining the relationship between scattered intensity and the quantity of scattering material. The complexity of the process is due to the fact that the scattering cross section is affected by the size, shape, concentration and composition of the scattering material, and by the characteristics of the acoustical beam. For the present study, attention is focused on determining the backscatter cross section of natural sand grains experimentally.

Two experimental methods can been applied for ultrasonic determination of scatterer size and concentration. One is the multiple-frequency technique using many narrow-band pulses each at a different discrete frequency. This method has been used in the ocean for zooplankton measurements (Greenlaw and Johnson, 1982. Holliday, 1987) and for suspended sediment measurements (Sheng, 1990, Sheng and Hay, 1991). The other method involves using

broadband pulses, in which a singe short pulse of wide bandwidth is used to increase the information content per pulse of the scattered ultrasound. This method has been used to study sand scattering by single elastic spheres (Dragonette et al., 1974). Broadband systems open the possibility of characterizing with a single transducer both the scatterer size distribution and concentration by an analysis of the amplitude and frequency content of the scattered waves. A good understanding of the factors influencing the generation, propagation, scattering, and reception of broadband ultrasonic pulses is needed to obtain quantitative information on the size and concentration parameters. The major parameters involved in the particle-ultrasound interaction are: the frequency-dependence of the total and differential scattering cross sections, particle concentration, and the scatterer size distribution.

1.2 Historical Background

Backscattering problems involving spherical geometries (i.e. solid sphere, Faran, 1951, spherical shells, Werby and Gaunaurd, 1987, coated shells, Gaunaurd and Kalnins, 1982, etc.) have been treated for the last 50 years. These problems are made nontrivial by the statistical nature of scattering

from an ensemble of scatterers (Marshall and Hitschfield, 1953) as well as by influences such as the grain size, shape, and orientation, and the quality of the grain boundaries (Varadan et al., 1985). The statistical variability can be removed by proper signal averaging, but the deterministic problem of individual scatterer cross section measurement or computation is much less tractable.

The principle and methods for backscattering measurement in solids and in water are similar, but the density of the scatterers in solids is much larger than in water. Research efforts for the backscattering problem in solids have been directed at characterizing the statistical relationships between the energy of the ultrasonic wave propagation and the local variation of the scatterers because of many random physical parameters, such as grain size, grain shape, grain orientation, quality of grain boundaries, the proportion of chemical constituents, and multiple scattering among grains. Beecham (1966) was able to demonstrate that the attenuation of backscattered echoes with distance in metals is related to the average grain size of the specimen. Aldridge (1969) confirmed Beecham's results and concluded that the distribution of grain scattering cross sections can be obtained through multiple measurement of nonoverlapping scattering regions. Fay (1973) and Goebbels et al. (1984)

further improved this idea to more accurately determine the expected amplitude of the backscattered echoes with respect to depth by utilizing various averaging techniques, namely spatial, directional, and frequency averaging which can also be used for suspended particle measurement in water.

The approach taken by bioacousticians has been to either model acoustical properties of biological scatterers as a compressible fluid sphere (Johnson, 1977, Greenlaw, 1982) or to use a semi-empirical approach based on laboratory measurements of typical cross sections (Love, 1977).

For work on acoustic scattering by suspended sand particles, because the distances between the scatterers usually are much larger than in solids, and sand particles are not so irregular as biological scatterers, the multiple scattering could be ignored. The approach was then to model sand particles as solid spheres of different materials. The scattering and backscattering cross sections of single particle or sand clouds can be calculated theoretically and measured in laboratory. Theoretical calculations of scattering by nonbiological particulates have been approached primarily through elastic or rigid material ("elastic" means that shear and compression waves may propagate within the material, and a "rigid" material in one in which no sound propagation occurs.) spheres (Hickling, 1962, Hay and Mercer, 1985), ellip-

soidal shapes (Peterson et. al., 1980), or slightly more complicated shapes such as cylinders with spherical end-caps (Numrich et al., 1981). Sheng and Hay (1988) compared the available data for scattered acoustic intensity and attenuation in dilute aqueous suspensions of sand with the theory. In the theoretical calculations, the scatterer was assumed to be spherical, and either elastic, or rigid and movable, or rigid and immovable. (An immovable particle is infinitely dense.) The results showed that the rigid movable model provided the best fit to the data, but that the total scattering cross sections were still larger than theory.

One important application of sand grain measurements is to estimate sediment transport. Dietz in 1948 first suggested a method for obtaining estimates of suspended sediment concentration in the ocean by measuring ultrasonic scatter. Flammer (1962) measured the frequency dependence of ultrasonic attenuation for many different sand size fractions in the sound frequency range of 2.5 to 25 MHz. His results were encouraging as regards the possibility of measuring the concentrations of the actual sand if its size distribution was known. Jansen et al. (1977,1979) developed an ultrasonic Doppler scatterometer. On similar principles, various acoustical measurement systems, such as ABSS (Acoustical Backscattering System, Hess and

Orr, 1979; Orr and Hess 1983; Hess and Bedford, 1985; Lynch 1985; Lynch et al., 1991; Lynch and Agrawal, 1991), ACM (Acoustic Concentration Meter, Young et al., 1982; Hanes et al. 1988; Vincent and Green, 1990; Thorne et al., 1991), UDS (Ultrasonic Doppler Scatterometer, Schaafsma et al., 1985), and the RASTRAN system (Hay et al., 1988; Hay, 1991) were developed for measuring concentrations and sizes of suspended particles. Hay (1983) employed a 192 kHz acoustical backscatter system to measure suspended sediment in a negatively buoyant, mine-tailing discharge plume in a submarine channel.

All of these studies have demonstrated the utility of acoustical remote sensing techniques with respect to the sediment transport problem. One of the remaining difficulties in the quantitative use of these techniques is to determine the acoustic backscatter cross section of natural sand precisely, which is needed to invert the backscattered signal to actual sediment concentration and size. The purpose of the work presented here is to investigate the use of broadband systems for suspended particle backscatter cross section measurement, in order to provide higher resolution measurements of the cross section than obtained previously.

1.3 The Approach in This Thesis

All of the investigations of sand particles measurement mentioned above employed narrowband transmissions. In this thesis, we try a different approach in which a broadband pulse is used. This permits measurement of the scattering cross section of natural sand grains at higher resolution in frequency than can be readily achieved with a narrowband system. Dragonette et al. (1974) investigated the relation between the reflected acoustical pressure and frequency for single elastic spheres of aluminum, brass, and tungsten carbide in water by using a broadband transducer in the transducer farfield. In the farfield, the detected volume is sufficiently far from the transducer that the piston may be considered a point source, the power in the beam decreases as the reciprocal of the square of the distance and the distribution of power with angle and distance is much more complicated. The measurements presented here are made in the nearfield of the transducer, because in the nearfield the changes in beam diameter with frequency are small and the power averaged over the beam diameter is approximately independent of distance from the transducer. This means that the changes in beam directivity pattern with frequency that are present in the farfield of a broadband

transducer need not be taken into account in the nearfield.

In order to understand the characteristics of the acoustical nearfield, the nearfield acoustical pressure is calculated theoretically in chapter 2 of this thesis. The case in which the vibration amplitude on the surface of the transducer is not uniform across this surface is considered, and represents an extension of previous work.

In chapter 3, we present measurements of the variations in the amplitude spectrum of the pulse reflected from an air-water interface as a function of distance in the nearfield of the transmitter. These measurements are compared with the theoretical results for the average acoustical pressure on the receiver surface from Chapter 2. The results are used to obtain estimates of the overall system sensitivity constant as a function of frequency, which are needed for the determination of absolute scattering cross sections.

In chapter 4, beginning with backscattering from a sphere, we obtain a relation between the receiver output and the concentration, average size and backscatter cross section for suspended particle clouds illuminated by a broadband acoustical beam in the nearfield.

The experimental measurements of the backscatter cross section of suspended sand are presented in chapter 5. These are new results, representing

the first suspended particle backscatter cross section measurements with a broad band system.

Chapter 6 consists of conclusions.

Chapter 2

THEORY OF NEARFIELD BEAM PATTERNS

2.1 Background and Basic Theory

In order to obtain consistent measurements of size and concentration of suspended particles in nearfield, the diffraction effects related to the finite aperture of the transducer and the characteristics of the acoustical field affected by the velocity distribution on the source surface should be investigated in detail. The problem of the baffled piston radiator has been very widely studied for various applications. The complete description of the

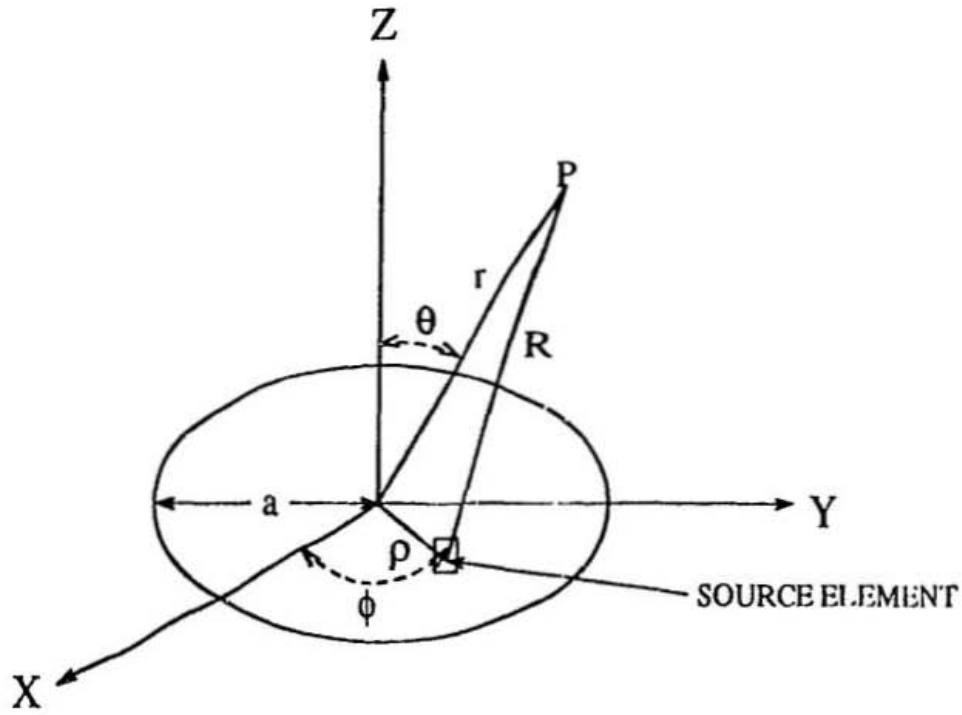

Figure 2.1: Geometry of circular piston

sound field produced by an acoustic piston is generally divided into two separate parts. One part of the description is limited to the region in the neighborhood of the piston, i.e. in the nearfield region, while the other part is confined to the farfield, the region beyond the nearfield. Because of the complex nature of the beam pattern close to the piston, especially for large ratios of radiator diameter to wavelength, the expression for the sound pressure within this area is complex and the integration of the equation for pressure becomes almost impossible to perform explicitly. Therefore this problem is usually solved by numerical methods.

There are several exact expressions for the field which are used in dealing with this problem. They all represent solutions to the equation (coordinate

system for this section refers to Fig. 2.1)

$$(\nabla^2 + k^2)\varphi = 0\,, \tag{2.1}$$

which satisfy the boundary condition $\frac{\partial \varphi}{\partial n} = g(\rho)$, $\rho < a$ and $\frac{\partial \varphi}{\partial n} = 0, \rho > a$ on the boundary. Here ∇^2 is Laplace's operator. n, ρ, a and $g(\rho)$ are normal direction, radial coordinate, piston radius and velocity distribution of piston surface respectively, φ is the velocity potential, and k is the wave number.

One of the expressions for the nearfield is that due to King (1934), who derives his relation from a generalized solution in cylindrical coordinates obtained by Bateman (1914). It is given by

$$\varphi = v_0 a \int_0^\infty e^{-\mu z} J_0(\mu\rho) J_1(\mu a) \frac{d\gamma}{\mu}\,, \tag{2.2}$$

where φ is the velocity potential at the field point P, $v_0 = \frac{\partial \varphi}{\partial n}$ is the normal velocity on the source surface which is uniform, and $\mu = (\gamma^2 - k^2)^{\frac{1}{2}}$, where γ and μ are separation constants (Harris, 1981). $J_0(\mu\rho)$ and $J_1(\mu a)$ are the zeroth and first-order cylindrical Bessel functions. On the baffle outside $\rho = a$, the normal velocity is zero. Williams (1951) and Greenspan (1979) used this expression to compute the nearfield of a circular piston.

Another expression is based on the time-domain Green's-function approach. The velocity potential due to a piston occupying a region s of a rigid

planar baffle is given by

$$\varphi = -\int_{-\infty}^{\infty} \int\int_{s} v_0(t') \frac{\delta(t - t' - \frac{R}{c})}{2\pi R} ds dt' \,. \tag{2.3}$$

R is the distance from the observation point P to the surface element ds. Lockwood and Willette (1973) used this expression to compute 3-dimensional graphs for the nearfield numerically.

The third exact expression to be mentioned here is the oldest, and probably the best known. It was introduced by Rayleigh (1945) in the late 1800's according to the Huygens' principle and takes the form

$$\varphi = \frac{1}{2\pi} \int\int_{s} \frac{v_0 e^{ikR}}{R} ds \,, \tag{2.4}$$

This equation was used by Seki (1954) and Zemanek (1971) for calculating the nearfield.

Numerical integration is usually required to calculate sound pressure in the nearfield. However, for some cases especially at large ratios of source diameter to the wavelength and at places very close the piston face, it is hard to obtain accurate results by numerical methods because the integrated function changes very rapidly. More effective methods (e.g. Cavanagh 1980, Ma 1987), using expansions or transformations were therefore developed.

For real situations, the distribution of velocity on the surface of the piston will not be uniform. If the crystal displacement is dominated by the first mode of vibration (i.e. there is no nodal circle on the vibrating surface except at the edge), the velocity on the surface of the piston should increase from the edge to the center, the maximum being at the center. Dekker et al. (1974) and Greenspan(1979) considered both simply-supported and clamped disks. For a disk with simply supported edges, radial vibration of the disk is everywhere possible, but axial displacements at the edge resting on the support are zero. The velocity distribution can be expressed by $v_0 = V_0[1-(\frac{\rho}{a})^2]$. For a disk with clamped edges, radial displacements and axial displacements at the clamped boundary both vanish. The velocity distribution can be written as $v_0 = V_0[1-(\frac{\rho}{a})^2]^2$ (for definition of different edge cases, see Timoshenko and Young, 1955). Timoshenko and Young discussed the effect of the velocity distribution at the source surface on the ultrasonic-beam characteristics along the axis of such a piston. However, using only axial changes it is difficult to understand how the acoustical behaviour in the whole nearfield is affected by the velocity distribution at the source.

Guyomar and Powers (1985) did another interesting piece of work. They calculated the acoustical pressure in the nearfield produced by a piston em-

bedded in: (1) free-space; (2) a rigid baffle which insulates the sound wave interference between front and back transducer; and (3) a resilient baffle. The calculation was performed in the angular spectrum domain and the results show that the acoustical pressure is seriously affected by the type of baffle.

Up to now, no exact calculation of the acoustical pressure for the continuous wave case in the whole nearfield, including nonuniform velocity distribution on the source surface, has appeared in the literature. Based on the work of Hasegawa et al. (1983,1984), which treated the transducer as a rigid piston with uniform normal velocity at its surface, this thesis presents the derivation of a formula for calculating the nearfield sound pressure of a circular piston with nonuniform velocity distribution. Three-dimensional graphs are used to show the acoustical pressure in the nearfield and to compare results with those produced by a transducer of uniform surface velocity. The effects of the surface velocity distribution in the nearfield are discussed and some physical explanations are given. At the same time, results obtained here are compared with those obtained using numerical methods.

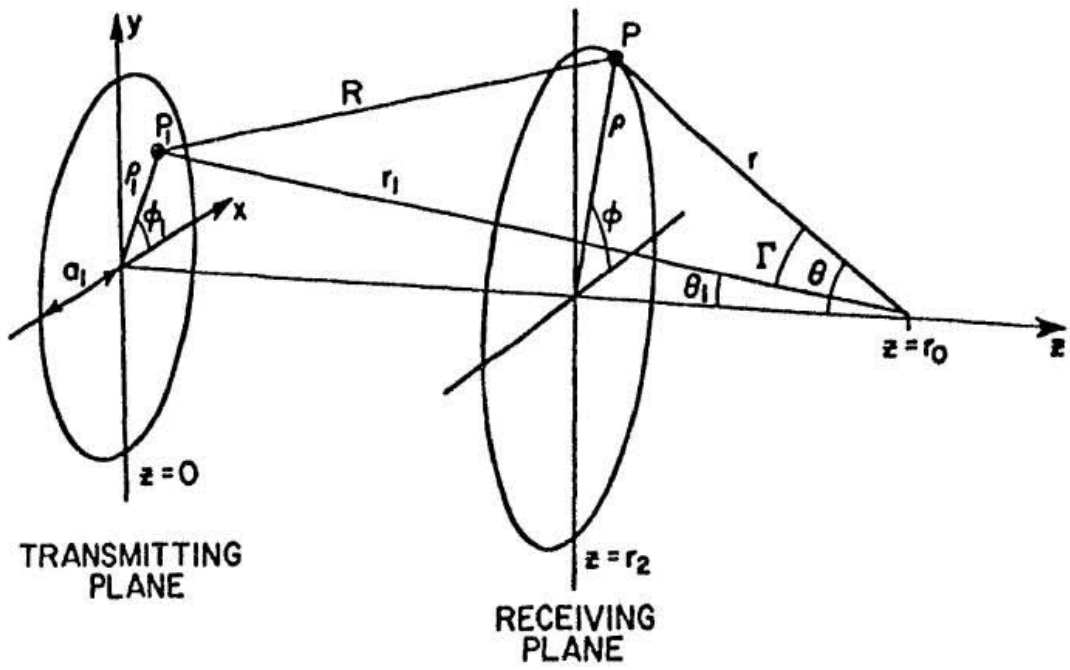

Figure 2.2: Coordinate system

2.2 General Theory

2.2.1 Case of Uniform Radiator

Because some results in the Hasegawa et al. (1983,1984) papers will be used later, in this section we briefly review their work .

The coordinate system is shown in Fig. 2.2. The origin of the cylindrical coordinate system is at the center of the piston where $z = 0$, while the spherical coordinate system origin is taken at $z = r_0$ on the axis of symmetry. The

velocity potential, φ, at a field point, P, for a plane piston source surrounded by an infinite rigid baffle is given by

$$\varphi = \frac{1}{2\pi} \int\int_{s_1} v_0 \frac{e^{-ikR}}{R} ds_1 \ . \tag{2.5}$$

where v_0 is the normal velocity at the piston surface. R is the distance from the field point to the surface element ds_1 on the piston, and is given by

$$R^2 = r^2 + r_1^2 - 2rr_1 \cos\Gamma \ . \tag{2.6}$$

and

$$\cos\Gamma = \cos\theta \cos\theta_1 + \sin\theta \sin\theta_1 \cos(\phi - \phi_1) \ . \tag{2.7}$$

For the case of relative sound pressure and uniform velocity distribution on the source surface, the constant $\frac{v_0}{2\pi}$ in equation (2.5) can be ignored and the equation rewritten as

$$\varphi(r,\theta) = \int\int_{s_1} \frac{1}{R} e^{-ikR} ds_1 \ . \tag{2.8}$$

By applying the relation (Arfken, 1970, p.768)

$$\frac{e^{-ik(r^2-2rr_1\cos\Gamma+r_1^2)^{\frac{1}{2}}}}{(r^2-2rr_1\cos\Gamma+r_1^2)^{\frac{1}{2}}} = -ik\sum_{n=0}^{\infty}(2n+1)j_n(kr)h_n^{(2)}(kr_1)P_n(\cos\Gamma) \ , \quad r < r_1 \tag{2.9}$$

where j_n is the spherical Bessel function, $h_n^{(2)}$ is the spherical Hankel function of the second kind, and P_n is the Legendre polynomial, equation (2.8) can be rewritten as

$$\varphi(r,\theta) = -ik\sum_{n=0}^{\infty}(2n+1)j_n(kr)\int\int_{s_1} h_n^{(2)}(kr_1)P_n(cos\Gamma)ds_1 \ , \qquad (2.10)$$

where $ds_1 = \rho_1 d\rho_1 d\phi_1 = r_1 dr_1 d\phi_1$ because of the relation

$$r_1^2 = \rho_1^2 + r_0^2 \ . \qquad (2.11)$$

According to the addition theorem (Arfken, 1970, p582) for Legendre polynomials, it follows that

$$\begin{aligned} & P_n[\cos\theta\cos\theta_1 + sin\theta sin\theta_1\cos(\phi-\phi_1)] \\ & = P_n(\cos\theta)P_n(\cos\theta_1) + 2\sum_{m=1}^{n}\frac{(n-m)!}{(n+m)!} \\ & P_n^m(\cos\theta)P_n^m(\cos\theta_1)\cos m(\phi-\phi_1) \ , \end{aligned} \qquad (2.12)$$

where P_n^m is the associated Legendre function of the first kind. Integrating both sides of the above equation with respect to ϕ from 0 to 2π, we have

$$\begin{aligned} & \int_0^{2\pi} P_n[\cos\theta\cos\theta_1 + sin\theta sin\theta_1\cos(\phi-\phi_1)]d\phi_1 \\ & = \int_0^{2\pi} P_n(\cos\Gamma)d\phi_1 \end{aligned}$$

$$= 2\pi P_n(\cos\theta)P_n(\cos\theta_1) \tag{2.13}$$

Therefore equation (2.10) becomes:

$$\varphi(r,\theta) = \frac{-2\pi i}{k}\sum_{n=0}^{\infty}(2n+1)j_n(kr)P_n(\cos\theta)f_n(Z_0, Z_1)\,. \tag{2.14}$$

where

$$f_n(Z_0, Z_a) = A_n(Z_a) - A_n(Z_0)\,, \tag{2.15}$$

$Z_0 = kr_0$, $Z_a = kr_a$, and r_a is the distance from the rim of the transmitter to the origin of the spherical coordinate system (Fig. 2.2). The A_n are given by the indefinite integral

$$A_n(Z) = \int Zh_n^{(2)}(Z)P_n(\frac{Z_0}{Z})dZ\,. \tag{2.16}$$

and satisfy the relations (Hasegawa et al., 1983)

$$A_n(Z) = -ZP_n(\frac{Z_0}{Z})h_{n-1}^{(2)}(Z) + \sum_{m=1}^{[\frac{n}{2}]}(-1)^{m+1}(2n-4m+1)P_{n-2m}(\frac{Z_0}{Z})h_{n-2m}^{(2)}(Z)\,,\ n \geq 2 \tag{2.17}$$

$$A_n(Z) + A_{n-2}(Z) = -Zh_{n-1}^{(2)}(Z)[P_n(\frac{Z_0}{Z}) - P_{n-2}(\frac{Z_0}{Z})]\,, \tag{2.18}$$

$$A_n(Z_0) + A_{n-2}(Z_0) = 0 \tag{2.19}$$

Here $[\frac{n}{2}]$ means the integer part of $\frac{n}{2}$. For a piston with a uniform velocity distribution, the above formula can be used for calculating the acoustical

pressure distribution in the nearfield. However, the boundary conditions imposed upon the crystal are one factor which will affect the velocity distribution. We will consider this problem below.

2.2.2 Simply Supported Radiator

Now we will consider the problem of nonuniform velocity distribution on the radiator. This may, in some applications, be more realistic than a uniform velocity distribution. For instance, a piezoelectric crystal, as it is used in ultrasonic transducers to measure suspended particles, fixed at the edges and backed with a damping material, will not move as a piston but will have a velocity distribution that is a minimum at the edge and a maximum at the center. In the case of ultrasonic transducers, experimental evidence indicates that the velocity profile has a nonuniform distribution rather than a uniform distribution (Shaw, 1956; Shaw and Sujir, 1960; Kikuchi. 1969)

Laura (1966) discussed the farfield beampattern produced by circular radiators with two different normal velocity profiles at the surface. One, called the simply supported case, is given by the expression

$$v_0(\rho_1) = \sum_{n=1}^{N} d_n[1 - (\frac{\rho_1}{a_1})^{2n}], \qquad (2.20)$$

and on the boundary.

$$v_0|_{\rho_1=a_1} = 0\,. \tag{2.21}$$

where the d_n are constants representing the weights for the different vibrational modes.

Another, which is called the clamped circular plate case, can be expressed as

$$v_0(\rho_1) = \sum_{n=2}^{N} c_n[1 - (\frac{\rho_1}{a_1})^2]^{2n}\,. \tag{2.22}$$

which satisfies the boundary conditions

$$v_0(\rho_1)|_{\rho_1=a_1} = 0\,,$$

$$\frac{dv_0(\rho_1)}{d\rho_1}|_{\rho_1=a_1} = 0\,.$$

Here c_n has the same meaning as d_n. These expressions constitute accurate approximations for the normal velocity of a circular radiator(Laura, 1966). For both cases, they represent a central maximum normal surface velocity and zero velocity at the edge. From the shapes of the sound pressure distribution on the acoustic axis (Dekker et al., 1974 and Greenspan, 1979), it can be seen that they are similar for the two different cases. In order to easily calculate, here, only the simply supported circular plate is considered. The result for the clamped plate case can be obtained in the same way.

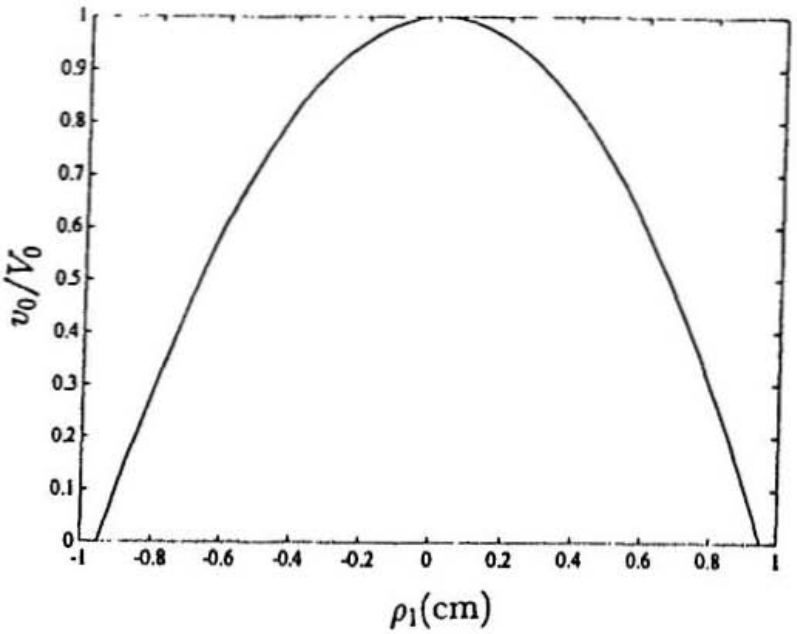

Figure 2.3: Velocity distribution on the piston surface for the transducer diameter used in the experiments

The following analysis is based on the assumption that the first mode of vibration dominates the crystal displacement. So the velocity distribution on the disk surface can be approximately expressed by the form shown in Fig. 2.3

$$v_0(\rho_1) = \begin{cases} V_0(1 - \frac{\rho_1^2}{a_1^2}) & \rho_1 < a_1 \\ 0 & \rho_1 \geq a_1 \end{cases} \tag{2.23}$$

Here v_0 is the surface normal velocity as before and V_0 is the surface velocity at the transmitter center, which is assumed to be unity for later

calculation. The relative velocity potential at the point P is now:

$$\varphi(r,\theta) = \int\int_{s_1} \frac{v_0(\rho_1)}{R} e^{-ikR} ds_1 \tag{2.24}$$

By using equation (2.11), the velocity on the surface of the piston becomes

$$v_0(r_1) = \begin{cases} [(1 + \frac{r_0^2}{a_1^2}) - \frac{r_1^2}{a_1^2}] & r_1 < (a_1^2 + r_0^2)^{\frac{1}{2}} \\ 0 & r_1 \geq (a_1^2 + r_0^2)^{\frac{1}{2}} \end{cases} \tag{2.25}$$

Substituting $v_0(r_1)$ into equations (2.24), and using equation (2.9) and equation (2.12) gives

$$\varphi(r,\theta) = \int\int_{s_1} \frac{[(1 + \frac{r_0^2}{a_1^2}) - \frac{r_1^2}{a_1^2}]}{R} e^{-ikR} ds_1$$

$$= \int\int_{s_1} [(1 + \frac{r_0^2}{a_1^2}) - \frac{r_1^2}{a_1^2}][-ik \sum_{n=0}^{\infty} (2n+1) j_n(kr) h_n^{(2)}(kr_1) P_n(cos\Gamma)] ds_1$$

$$= \int_{r_0}^{r_a} \{[(1 + \frac{r_0^2}{a_1^2}) - \frac{r_1^2}{a_1^2}][-ik \sum_{n=0}^{\infty} (2n+1)$$

$$j_n(kr) h_n^{(2)}(kr_1) \int_0^{2\pi} P_n(cos\Gamma) d\phi_1]\} r_1 dr_1$$

$$= -2\pi ki \sum_{n=0}^{\infty} (2n+1) j_n(kr) P_n(cos\theta) [(1 + \frac{r_0^2}{a_1^2})$$

$$\int_{r_0}^{r_a} h_n^{(2)}(kr_1) P_n(\frac{r_0}{r_1}) r_1 dr_1 - \int_{r_0}^{r_a} \frac{r_1^3}{a_1^2} h_n^{(2)}(kr_1) P_n(\frac{r_0}{r_1}) dr_1] . \tag{2.26}$$

For nonuniform velocity distribution on the surface of the piston, the velocity potential at the point P consists of two parts. The first part is seen

from the last section to be the expression for the case of uniform velocity distribution. The second part is the modifying term which is caused by the velocity changing on the piston surface. If we let

$$b_n(kr_0, kr_a) = k^4 \int_{r_0}^{r_a} r_1^3 h_n^{(2)}(kr_1) P_n(\frac{r_0}{r_1}) dr_1$$

$$= \int_{Z_0}^{Z_a} Z^3 h_n^{(2)}(Z) P_n(\frac{Z_0}{Z}) dZ$$

$$= B_n(Z_a) - B_n(Z_0) \tag{2.27}$$

where $Z_0 = kr_0$, $Z_a = kr_a$ as before and

$$B_n(Z) = \int Z^3 h_n^{(2)}(Z) P_n(\frac{Z_0}{Z}) dZ \,, \tag{2.28}$$

equation (2.26) can then be rewritten as

$$\varphi(r,\theta) = \frac{-2\pi i}{k} \sum_{n=0}^{\infty} (2n+1) j_n(kr) P_n(cos\theta) [(1+\frac{r_0^2}{a_1^2}) f_n(Z_0, Z_a) - \frac{1}{a_1^2 k^2} b_n(Z_0, Z_a)] \tag{2.29}$$

Equation (2.28) is solved using integration by parts and the relations (Arfken, 1970, *p.*525, *p.*540)

$$Z h_n^{(2)}(Z) = (2n-1) h_{n-1}^{(2)}(Z) - Z h_{n-2}^{(2)}(Z) \,, \tag{2.30}$$

$$(n+1) P_{n+1}(Z) - (2n+1) Z P_n(Z) + n P_{n-1}(Z) = 0 \,, \tag{2.31}$$

and

$$\int Z^{1-n} h_n^{(2)}(Z) dZ = -Z^{1-n} h_{n-1}^{(2)}(Z) . \tag{2.32}$$

Then, the first several successive $B_n(Z)$'s can be calculated analytically as follows (see Appendix):

$$B_0(Z) = (-Z^2 + i2Z + 2)e^{-iZ} \tag{2.33}$$

$$B_1(Z) = -Z_0(2 + iZ)e^{-iZ} \tag{2.34}$$

$$B_2(Z) = Z^2 A_2(Z) + 3Z_0 A_1(Z) - 4A_0(Z) + Z^2 h_0(Z) \tag{2.35}$$

$$B_3(Z) = Z^2 A_3(Z) + \frac{10}{3} Z_0 A_2(Z) - \frac{26}{3} A_1(Z) + \frac{4}{3} Z_0 Z h_1(Z) \tag{2.36}$$

$$\begin{aligned} B_4(Z) = Z^2[A_4(Z) - \frac{3}{4} A_2(Z)] - [10A_2(Z) - 2A_0(Z)] + \frac{3}{2} A_0(Z) \\ + \frac{7}{2} Z_0 A_3(Z) - \frac{15}{2} A_2(Z) + \frac{3}{4} B_2(Z) \end{aligned} \tag{2.37}$$

$$\begin{aligned} B_5(Z) = Z^2[A_5(Z) - \frac{4}{5} A_3(Z)] - 2[7A_3(Z) - 3A_1(Z)] + \frac{24}{5} A_1(Z) \\ + \frac{18}{5} Z_0 A_4(Z) - \frac{56}{5} A_3(Z) + \frac{4}{5} B_3(Z) \end{aligned} \tag{2.38}$$

$$\begin{aligned} B_6(Z) = Z^2[A_6(Z) - \frac{5}{6} A_4(Z)] - 2[9A_4(Z) - 5A_2(Z) + A_0(Z)] \\ + 2[\frac{25}{6} A_2(Z) - \frac{5}{6} A_0(Z)] + \frac{11}{3} Z_0 A_5(Z) - 15A_4(Z) + \frac{5}{6} B_4(Z) \end{aligned} \tag{2.39}$$

By use of these equations, the relation below can be obtained,

$$B_n(Z) = Z^2[A_n(Z) - \frac{(n-1)}{n}A_{n-2}(Z)] - 2\sum_{m=1}^{[\frac{n}{2}]}(-1)^{m+1}(2n-4m+1)A_{n-2m}(Z)$$

$$+\frac{2(n-1)}{n}\sum_{m=1}^{[\frac{n}{2}-1]}(-1)^{m+1}(2n-4m-3)A_{n-2m-2}(Z)$$

$$+\frac{2(2n-1)}{n}Z_0A_{n-1}(Z) - \frac{2(n-1)(2n-3)}{n}A_{n-2}(Z) + \frac{n-1}{n}B_{n-2} \quad n > 3 \tag{2.40}$$

Above equation can be further simplified by letting

$$g_n(Z) = \sum_{m=1}^{[\frac{n}{2}]}(-1)^{m+1}(2n-4m+1)A_{n-2m}(Z) \qquad n \geq 2 \tag{2.41}$$

and

$$g_0(Z) = g_1(Z) = 0 \tag{2.42}$$

to easily obtain

$$g_{n-2}(Z) = \sum_{m=1}^{[\frac{n}{2}-1]}(-1)^{m+1}(2n-4m-3)A_{n-2m-2}(Z) \qquad n \geq 2 \tag{2.43}$$

Then, the following recurrence formulas can be obtained

$$g_n(Z) + g_{n-2}(Z) = (2n-3)A_{n-2}(Z), \quad n \geq 2 \tag{2.44}$$

Substituting $g_n(Z)$ into equation (2.40) finally gives the recurrence formula for $B_n(Z)$ as

$$B_n(Z) = Z^2[A_n(Z) - \frac{(n-1)}{n}A_{n-2}(Z)] + \frac{2(2n-1)}{n}Z_0 A_{n-1}(Z) -$$

$$\frac{2(n-1)(2n-3)}{n}A_{n-2}(Z) - 2g_n(Z) + \frac{2(n-1)}{n}g_{n-2}(Z) + \frac{n-1}{n}B_{n-2}(Z) \, , n > 3$$

(2.45)

Using computer algorithms it is found that $B_n(Z)$ converges very rapidly. Since the computer can calculate recurrence formulas quickly, the velocity potential, $\varphi(r,\theta)$, can be evaluated very efficiently using equations (2.18), (2.47), (2.45), and (2.29) . Because no approximation is used in the derivation, the result calculated from equation (2.29) should be the exact solution. Equation(2.45) can be proved by differentiating its two sides with respect to z, and detailed procedure is given in Appendix B.

2.3 Nearfield of a Circular Piston

In order to investigate the nearfield region, the acoustical pressure which can be obtained from the velocity potential ($p = -\rho_0 \frac{\partial \varphi}{\partial t}$) is calculated, by use of the above equations, for points located on a grid in the x-z plane.The piston axis corresponds to the z coordinate (Fig. 2.2), and the orthogonal coordinate is x . For our case, the sound pressure is symmetric about the z

axis, so we only consider sound pressure in the plane of $x > 0$ and $z > 0$. the parameters we chose for calculating the acoustical field are the same as those used in our experiments.

The functions j_n, $h_n^{(2)}$, P_n, A_n, and B_n are calculated by use of recurrence formula. We chose the distance from the origin of the spherical coordinate system to the origin of the cylindrical coordinate system to be $r_0 = 22$ cm. The diameter of the piston is equal to 1.9 cm, the frequency f = 2.0 MHz and the speed of sound in water is taken to be 1483 ms^{-1}. We chose $r_0 = 22$ cm so that at places being larger than 0.2 cm from transducer surface they all satisfy relationship $r < r_1$ in equation (2.9).

Fig. 2.4 shows the sound pressure on the acoustical axis(i.e. the z axis). The dashed and solid curves, respectively, are the results with the nonuniform and uniform velocity distribution on the piston surface. For a circular piston with uniform velocity distribution on the surface, the last maximum appearing on the acoustical axis is determined by the equation (Clay and Medwin, 1977),

$$z_g = \frac{a_1^2}{\lambda}\,, \tag{2.46}$$

where a_1 is the piston radius and λ is the wavelength. For our case, $f \approx 2.0$

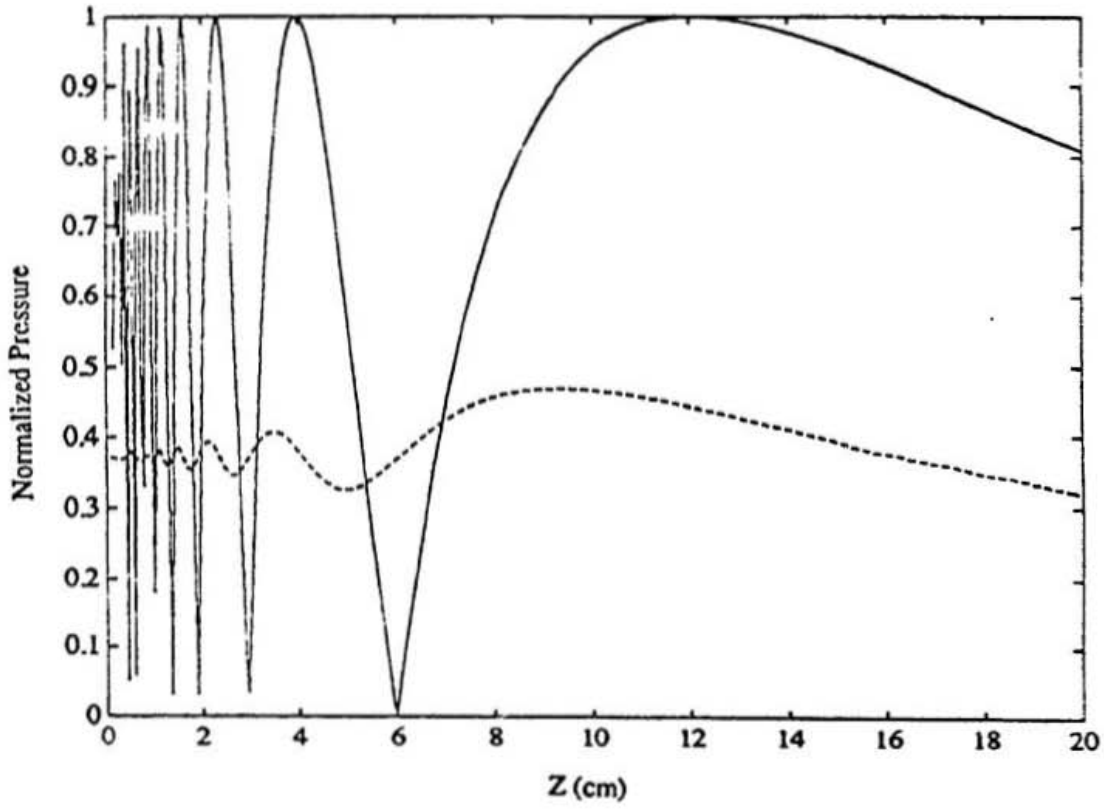

Figure 2.4: Acoustical pressure on the acoustical axis, f = 2.0 MHz

MHz and $\lambda \approx 0.7$ mm, this give

$$z_g \approx 12.2 \text{ cm} . \tag{2.47}$$

This can be seen from the solid curve in Fig. 2.4. While both curves in Fig. 2.4 show maxima and minima, it is evident that the amplitude of the dashed curve is very small compared with that of the solid curve. As well, there is no zero point for the dashed curve, and its last maximum point is nearer the piston surface than that of the solid curve (approximately $\frac{3}{4}\frac{a^2}{\lambda}$). All of these characteristics appear to be in good agreement with the results of Dekker et al. (1974) and Greenspan (1979).

Figures 2.5 and 2.6 are 3-dimensional graphs of acoustical pressure for uniform and non-uniform v_0 respectively. We can see that the interference pattern exists in both of them, but Fig. 2.6 looks much more regular and smooth. The differences between maxima and minima are smaller in Fig. 2.6 than in Fig. 2.5. These figures imply that through controlling velocity distribution, different spatial acoustical pressure fields can be obtained.

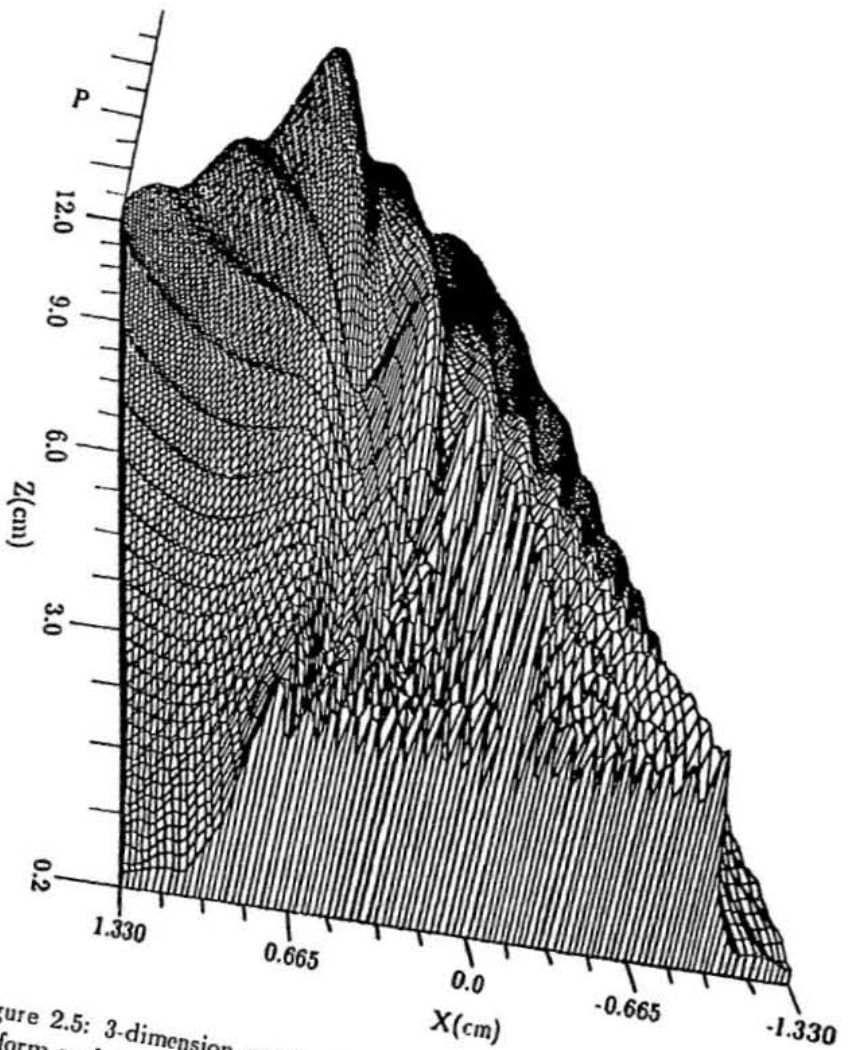

Figure 2.5: 3-dimension graph of acoustical pressure in the nearfield with uniform surface velocity

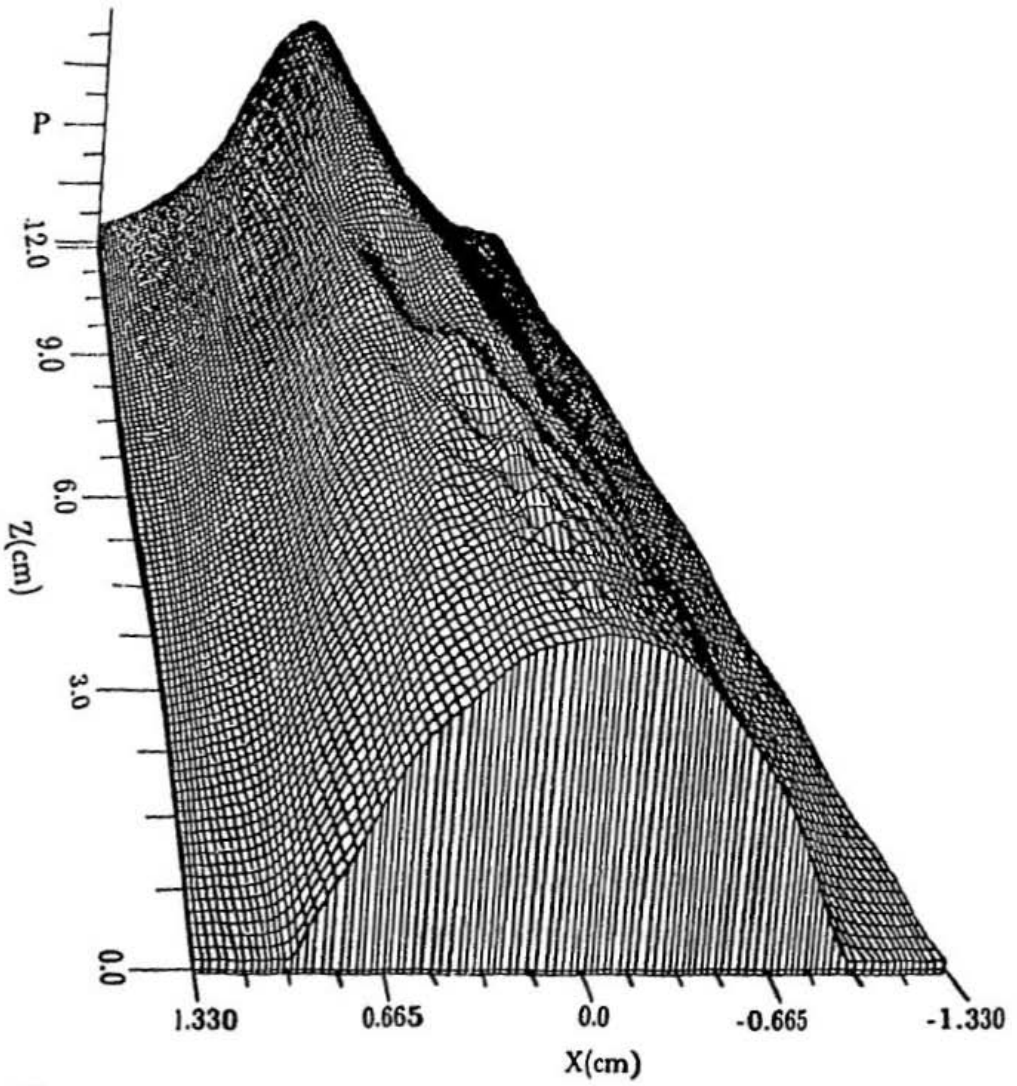

Figure 2.6: 3-dimension graph of acoustical pressure in the nearfield with nonuniform surface velocity

2.4 Space Average Pressure in the Nearfield

Since the output of a receiver is proportional to the average acoustical pressure acting on its surface, in practical applications, knowing how beamwidth and average pressure on the receiver surface change along the acoustical axis is often important. We will use the formulae obtained above to determine how the acoustical pressure on the plane which is perpendicular to the z axis changes with axial distance.

The coordinate system used in the calculations is the same as shown in Fig. 2.2. Assume the calculation is carried out for the plane $z = r_2$, and the space average value of p over the receiving crystal is

$$< p >= \frac{1}{s_2} \int \int_{s_2} p ds_2 \,, \tag{2.48}$$

where $ds_2 = \rho d\rho d\phi$, and s_2 is the receiving crystal area. From the relation

$$r^2 = \rho^2 + (r_0 - r_2)^2 \,, \tag{2.49}$$

the ds_2 is

$$ds_2 = r dr d\phi \,. \tag{2.50}$$

Substituting equation (2.29) into equation (2.48) gives (here we use pressure instead of velocity potential because the difference between them is just a

constant for the same frequency case)

$$< p >= \frac{-1}{ks_2}\{2\pi i \sum_{n=0}^{\infty}(2n+1)[(1+\frac{r_0^2}{a_1^2})f_n(Z_0, Z_1)$$

$$-\frac{1}{a_1^2k^2}b_n(Z_0, Z_1)]\int_{r_0-r_2}^{r_{a2}}\int_0^{2\pi} j_n(kr)P_n(\frac{r_0-r_2}{r})rdrd\phi\}\,. \qquad (2.51)$$

The integration factor can be simplified as

$$\int_{r_0-r_2}^{r_{a2}}\int_0^{2\pi} j_n(kr)P_n(\frac{r_0-r_2}{r})rdrd\phi$$

$$= \frac{2\pi}{k^2}\int_{k(r_0-r_2)}^{kr_{a2}} ZRe[h_n^{(2)}(Z)]P_n(\frac{Z_0}{Z})dZ$$

$$= \frac{2\pi}{k^2}Re[\int_{k(r_0-r_2)}^{kr_{a2}} Zh_n^{(2)}(Z)P_n(\frac{Z_0}{Z})dZ]$$

$$= \frac{2\pi}{k^2}Re[f_n(Z_0', Z_1')]\,, \qquad (2.52)$$

where $Z_0' = (r_0 - r_2)k$ and $Z_1' = r_{a2}k$ with r_{a2} being the distance from the rim of the receiving plane to the origin of the spherical coordinate system. Equation (2.51) then becomes

$$< p >= \frac{-1}{s_2k^3}4\pi^2 i\sum_{n=0}^{\infty}(2n+1)[(1+\frac{r_0^2}{a_1^2})f_n(Z_0, Z_1)-\frac{1}{a_1^2k^2}b_n(Z_0, Z_1)]Re[f_n(Z_0', Z_1')] \qquad (2.53)$$

Fig 2.7 shows the values of average acoustical pressure on receiving planes of

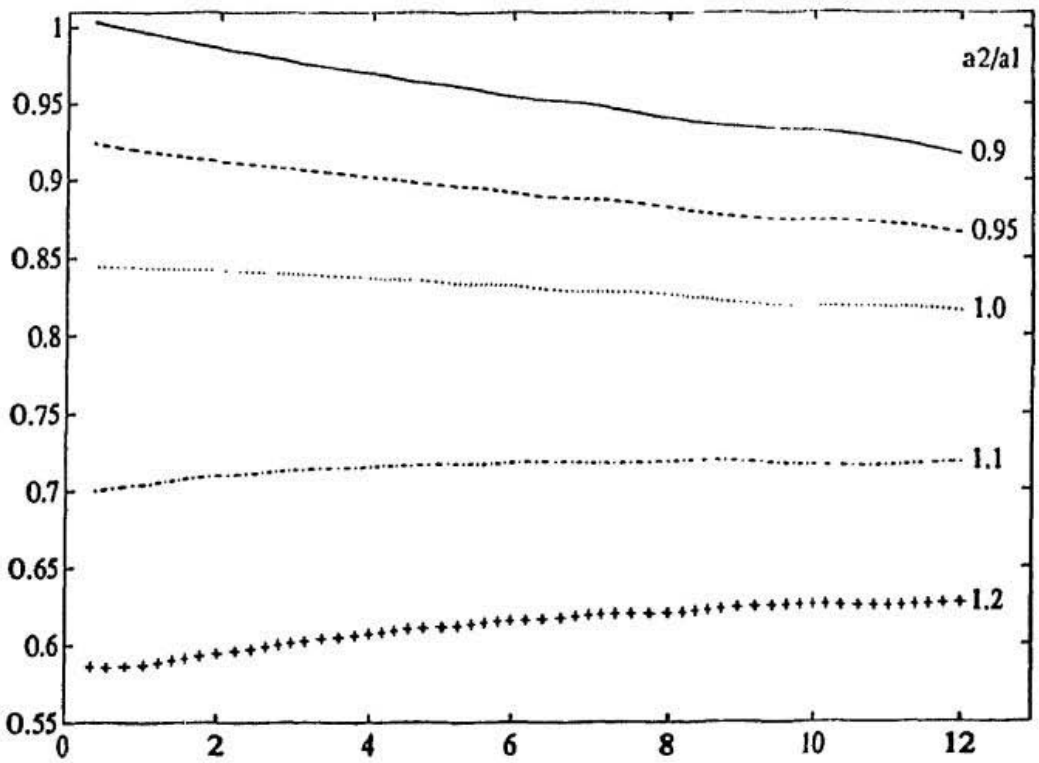

Figure 2.7: Average acoustical pressure on the different size of receiving surface (radius a2) produced by transmitter (radius a1) with the simply supported edge, at f = 2.0 MHz

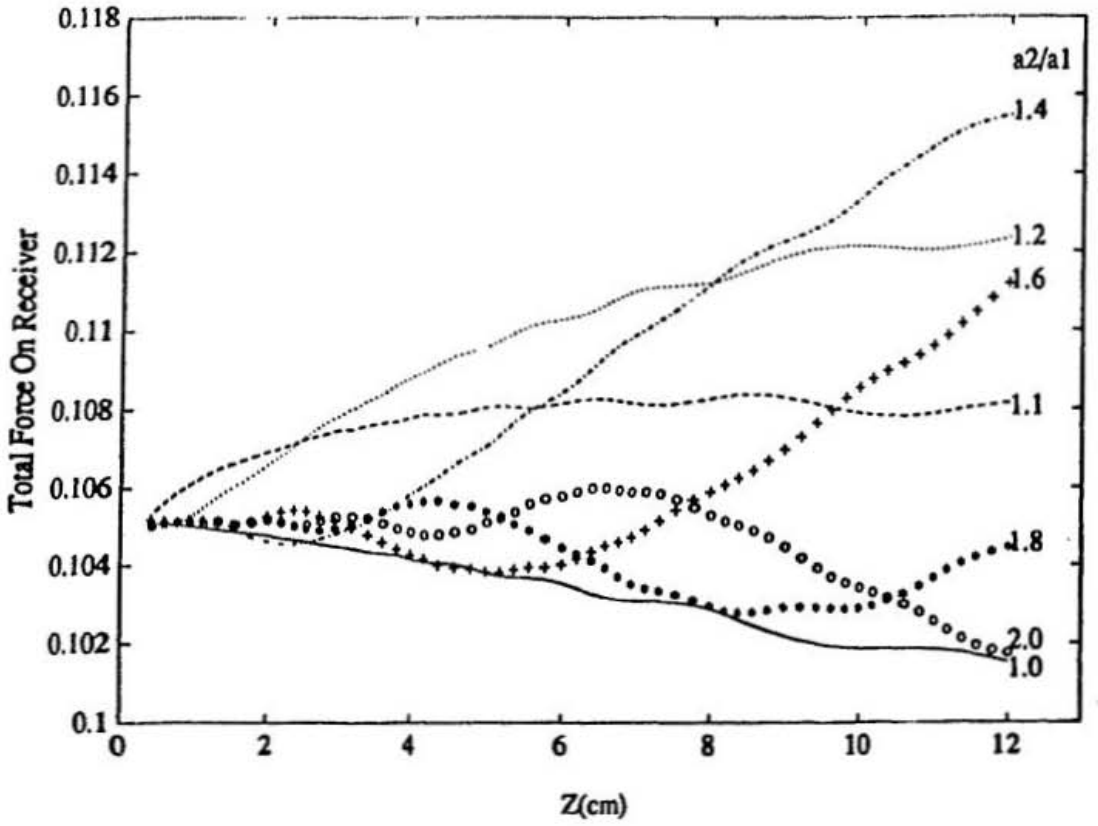

Figure 2.8: Total acoustical force on the different size of receiving surface (radius a2) produced by transmitter(radius a1) with the simply supported edge, at 2.0 MHz

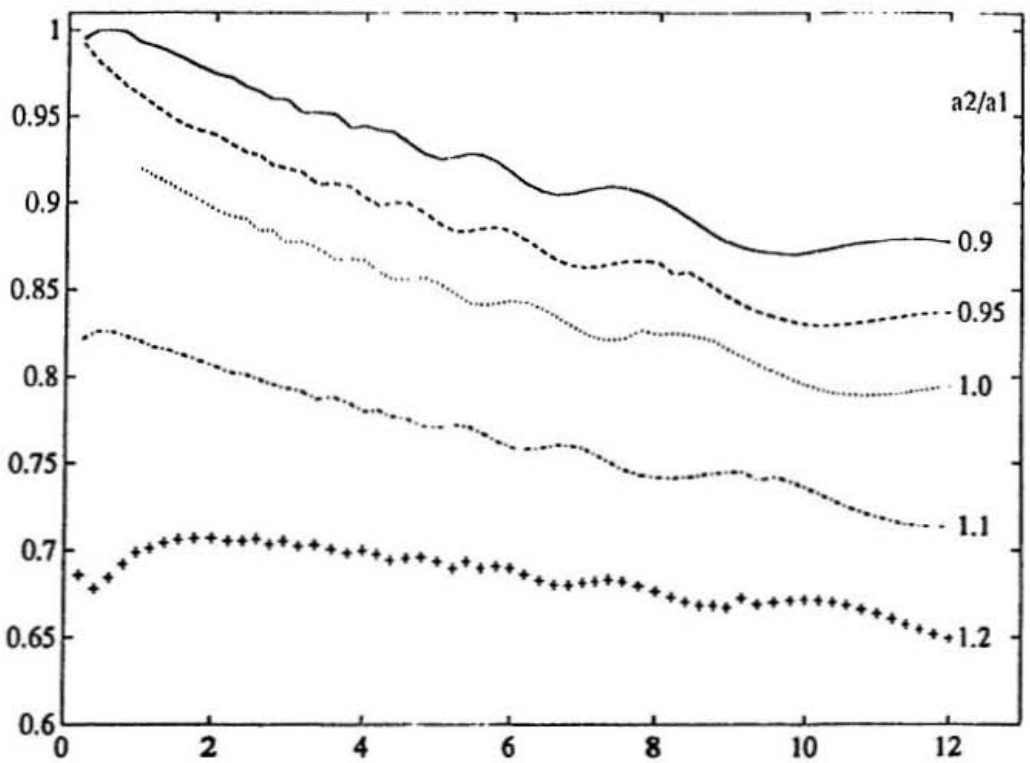

Figure 2.9: Average acoustical pressure on different size of receiving plane produced by transmitter with uniform surface velocity, at 2.0MHz

differing sizes as a function axial distance z. From these curves the following results can be obtained:

(1)Average values of pressure decrease with increasing radius, and this means that beam intensity concentrates around the acoustical axis z.

(2)When the radius of the receiving area is around 1.0 to 1.1 times that of the transmitting area, the average pressure along the acoustical axis is almost independent of z.

(3)When the radius of the receiving area is over 1.1 times that of the transmitting area the average acoustical pressure increases along the acoustical axis. This point is more easily seen from Fig. 2.8 in which the curves represent total acoustical force on the receiving plane and all parameters are the same as for Fig. 2.7. For $a_2 = 1.4a_1$, the total acoustical pressure reaches its maximum, and then it decreases again. This is because of the effects of diffraction and interference. Usually divergence of beamwidth is thought to be unimportant in the nearfield, but the curves in Fig. 2.8 suggest that it should not be ignored for some applications.

Fig. 2.9 shows results when v_0 is uniform. The parameters used are the same as those in Fig. 2.7. By comparing Figures 2.7 and 2.9, it is easily seen that the average acoustical pressure on the receiving area along the

acoustical axis changes less when the boundary condition for the simply supported radiator is applied. The slopes of the curves in Fig. 2.7 are also smaller than those in Fig. 2.9.

2.5 Comparison with Numerical Integration

The acoustical pressure in the nearfield expressed by equation (2.24) can be integrated numerically. In order to check our result and also to see whether a numerical method is really effective for the case of large ratio of source size to wavelength near the surface of the piston, we use the Gauss quadrature method (Press et al. 1986) to integrate equation (2.24).

The coordinates of the piston being considered are shown in Fig. 2.10. The piston has radius a_1, and vibrates with simple harmonic motion normal to its face. The observation point will be a function of r, the radial distance from the center of the piston, and θ, the angle between the piston axis and the radial vector. The total relative force can be written as in equation(2.24). The distance R is given by

$$R = (r^2 + \rho_1^2 - 2r\rho_1 sin\theta cos\phi_1)^{\frac{1}{2}} . \qquad (2.54)$$

Because of the axial symmetry of the problem, the total force on this plane

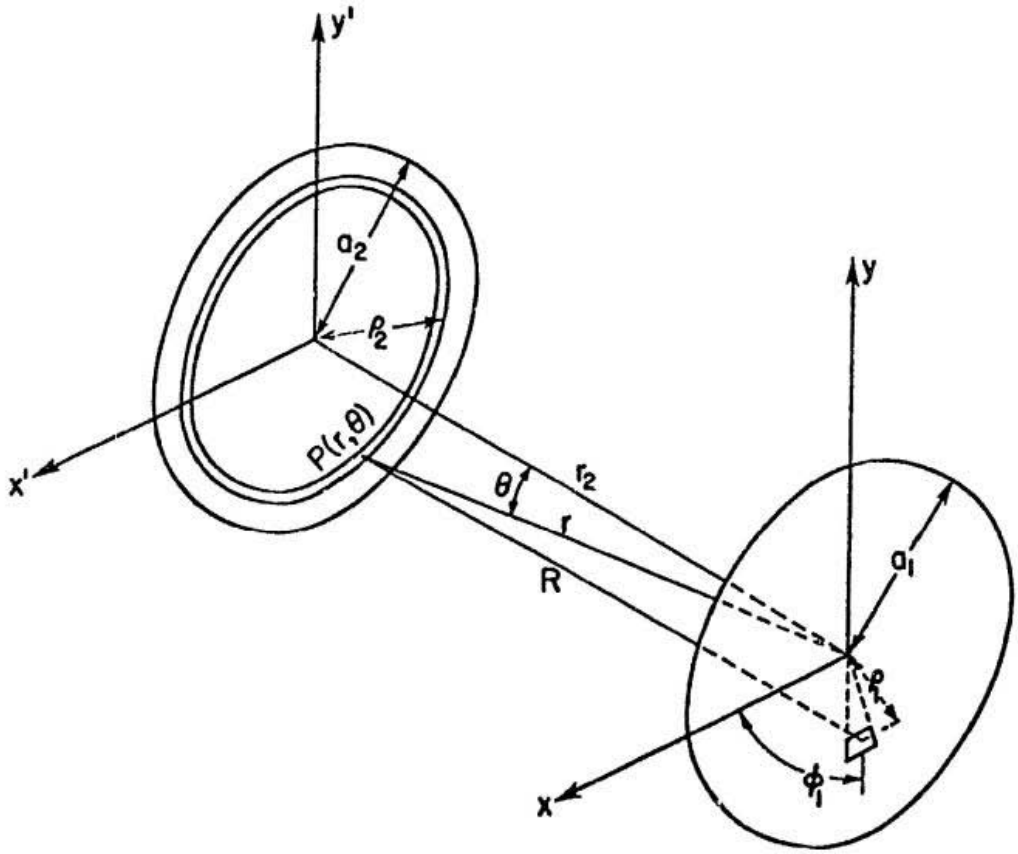

Figure 2.10: Coordinate system for numerical calculation

is

$$F_t(r_2) = \int_0^{a_2} p(r,\theta) 2\pi\rho_2 d\rho_2 \tag{2.55}$$

where a_2 is the radius of the receiver and as before, r_2 is the distance between the piston and the receiver. From Fig. 2.10 we may write

$$r = \frac{r_2}{\cos\theta} , \tag{2.56}$$

$$\rho_2 = r_2 \tan\theta . \tag{2.57}$$

and

$$d\rho_2 = \frac{r_2}{\cos^2\theta} d\theta . \tag{2.58}$$

Substituting the above into equation (2.55) and using equation (2.23) gives

$$F_t(r_2) = -i\omega 2\pi\rho_0 \int_0^{\tan^{-1}\frac{a_2}{r_2}} \int_0^{a_1} \int_0^{2\pi} e^{-ikR} \frac{r_2^2 \sin\theta \rho_1 (1 - \frac{\rho_1^2}{a^2})}{R\cos^3\theta} d\phi_1 d\rho_1 d\theta , \tag{2.59}$$

In Zemanek's (1971) paper, the piston is divided into $32\pi(\frac{a_1}{\lambda})^2$ elements in order to obtain results within 0.5% error. A piston of radius 0.95 cm and transmitting frequency of 2 MHz should thus be divided into at least 29475 elements. In order to get high accuracy results, 192 point Gauss quadrature is used for each of the three dimensions of integration. Therefore, the transmitting piston is divided into 36864 elements.

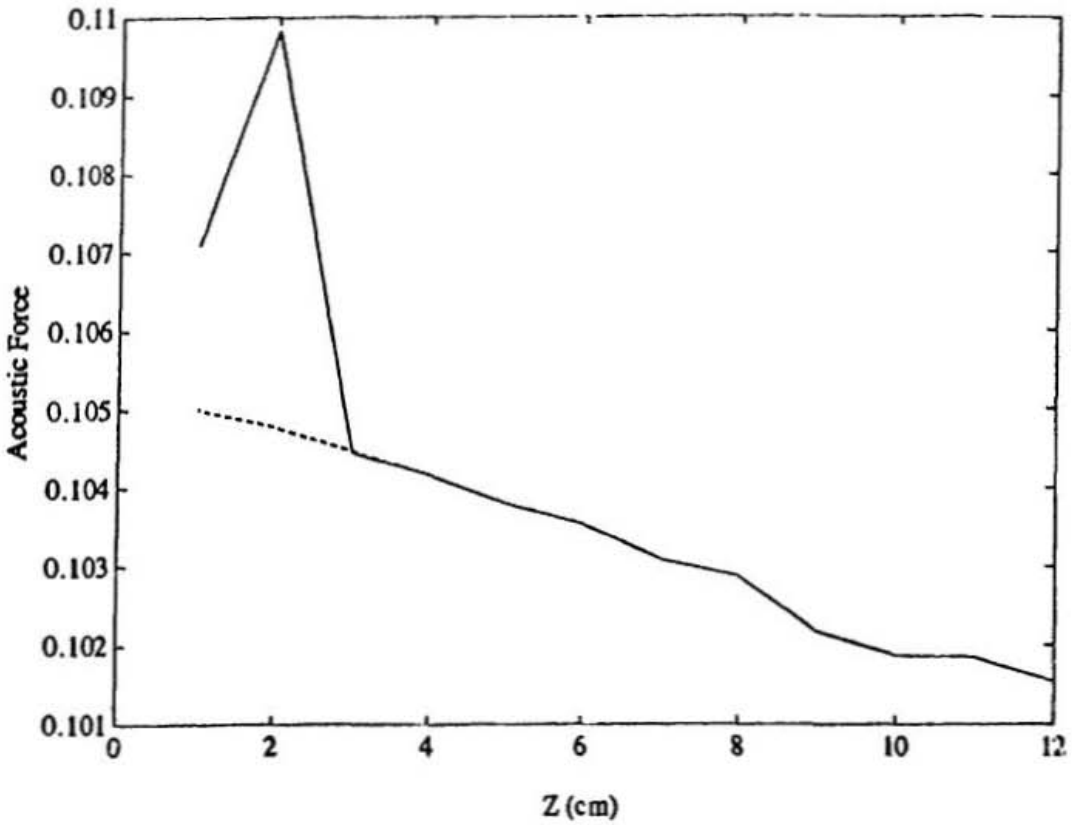

Figure 2.11: The total acoustical force on the receiving plane, for $a_1 = a_2$ and f=2.0MHz

In Fig. 2.11, the solid curve is obtained from equation (2.59), and the dashed curve is from equation (2.53). Near the surface of the piston the numerical result exhibits oscillatory behaviour. However, beyond about 2 cm the solid and dashed curves agree very well. The differences at close range are because interference is produced mainly by phase differences. The nearer an observed point is to the surface of the piston, the larger the phase difference between signals arriving from any two given elements of the source. It is difficult to get high accuracy results using numerical methods when evaluating rapidly varying functions. It can be seen from solid curve in Fig.(2.11), oscillations appear at places close to the transmitter surface. We have found that using more points in the calculation produces only slight changes in the results. For large ratios of radiator size to wavelength it is expected that the total force computed using equation (2.53) will behave better than numerical integration because for this case the nearfield changes very quickly. Another advantage of equation (2.53) is that the speed of calculation is very fast(around two times faster than numerical method for our case).

We have thus seen that, although the pattern of acoustical pressure in the nearfield is complex, by comparison the average pressure on the receiver

surface varies much less appreciably with changing distance along the acoustical axis . It is because of this that it is feasible to use backscatter from the nearfield to study particulate suspensions, provided that the scatterers are distributed uniformly on average across the width of the beam.

Chapter 3

MEASUREMENT OF SYSTEM CONSTANT AND ACOUSTICAL PRESSURE

In the previous chapter, we derived a theoretical result which shows that the velocity distribution on the surface of a transducer plays an important role in affecting the pressure field. For a real transducer, the operation of transducers may be affected by other variables, including the acoustical damping material, size, shape, orientation, and composition of the piezoelec-

tric element. These factors all influence the form of the transducer output in terms of the pulse shape and the spatial variations of the pressure amplitude. In addition to this internal variability among transducers, external factors such as the electrical properties of the pulser/receiver can play a role.

In view of this variability, it is important to characterize the transducer in terms of transmitting and receiving response function, without prior knowledge of the detailed internal structure of the transducer and its associated electronics. This is the purpose of our experiment in which the overall system sensitivity constant and the average pressure on the surface of a receiver changing with distance from the transmitter will be measured. The method to measure average pressure is to use the transducer in the pulse-echo mode, with the transducer itself being both the transmitter and receiver. This technique can yield amplitude, spectral and spatial information.

3.1 Measuring System

A glass-sided tank of 90cm(long)×30cm(wide)×42cm(high) was used for the measurements, and was filled with deionized water, as shown in Fig. 3.1. The tank was mounted on an adjustable support, and on the top of the tank

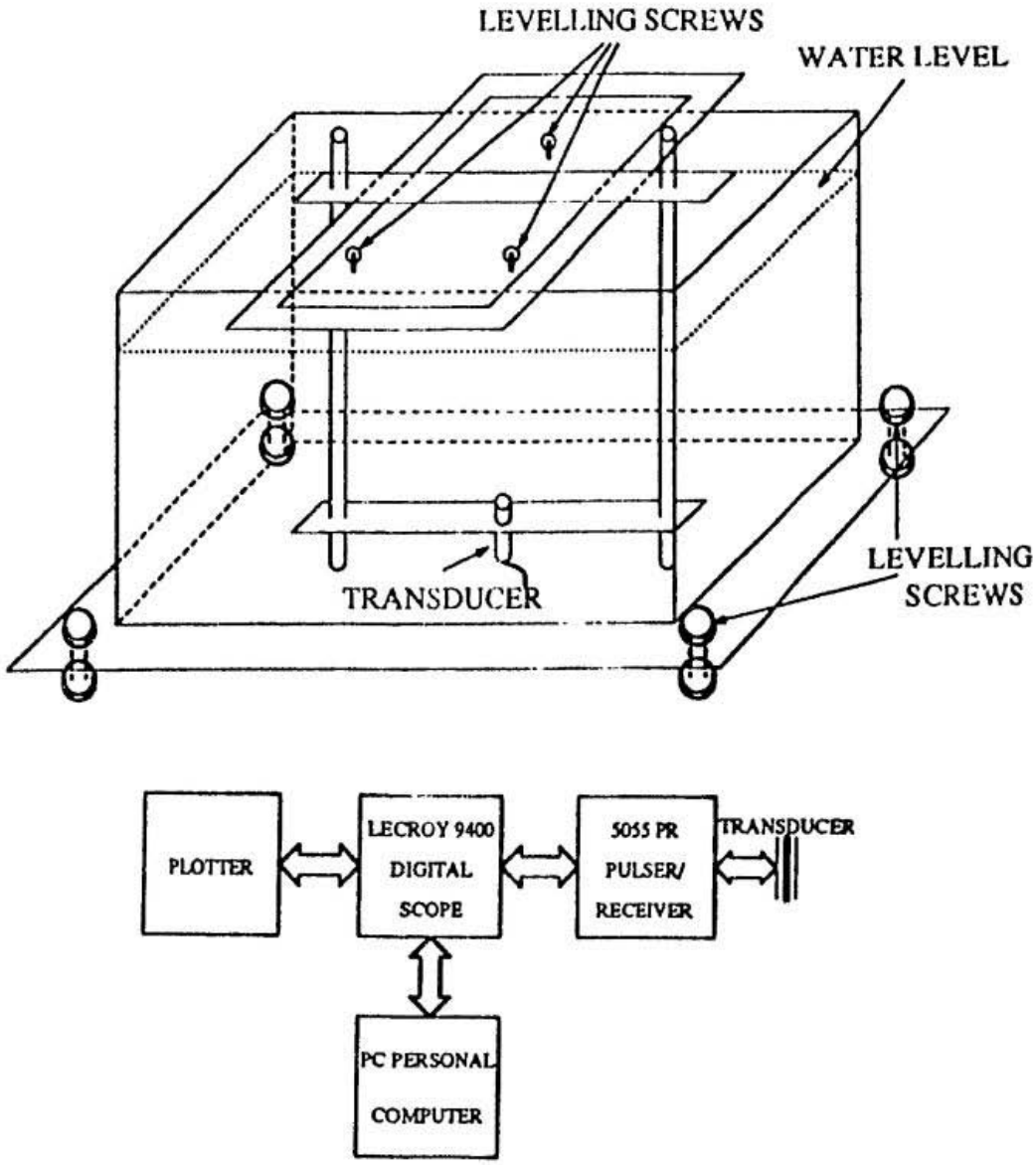

Figure 3.1: Sketch of experimental set up

there was another adjustable device which extended into water. To the latter was attached a 0.95 cm radius commercial broadband transducer which was used as the source and receiver. This disk was pointed upward towards the water air interface. The center, upper(-6dB), and lower(-6dB) frequencies of the transducer are 2.09 MHz, 2.82 MHz, and 1.36 MHz respectively. Thus, the bandwidth is around 69.9% of the centre frequency. Figure 3.2 shows a time-series and spectrum of the reflected pulse. The driving signal, a $2\mu s$ voltage pulse, is generated by a Parametrics $5055PR$ pulser/receiver. This had a typical rise time of 20ns when driving a purely resistive 50 Ω load. The shape of the emitted ultrasonic waveform could be varied by adjusting the energy and damping controls of the unit. The sampling time is $10\mu s$, giving a 0.1 MHz frequency resolution and 0.75cm spatial resolution. Received time-domain signals were recorded by a digital oscilloscope (LeCroy 9400) which was connected to a personal computer and plotter through a GPIB interface. The LeCroy 9400 has two independent channels, each providing an 8-bit sampling A/D converter up to 100 MHz sampling rate and 4k length of memory. Two other function memories permit Fast Fourier Transform (FFT), averaging and other operations to be performed. Therefore, it is possible to do some data processing before the data are transferred to the

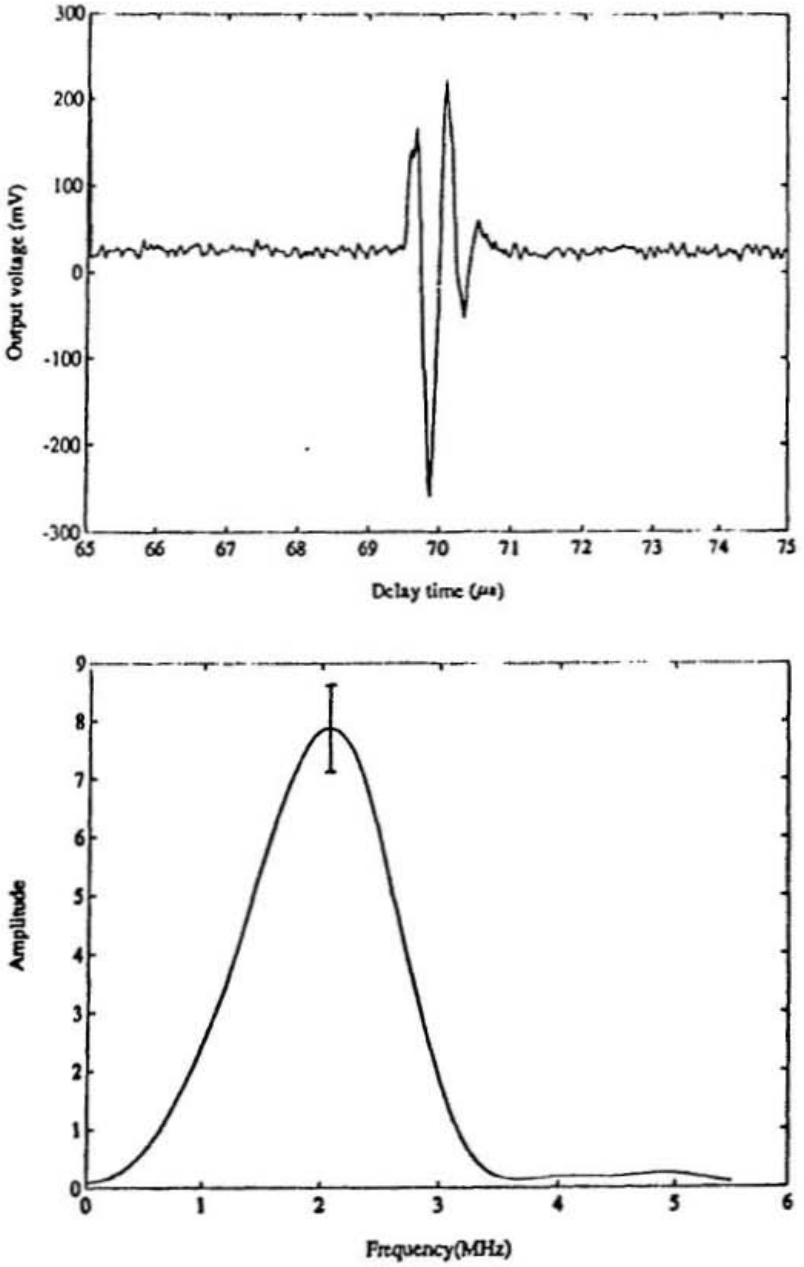

Figure 3.2: Time-series and spectrum of the reflected pulse

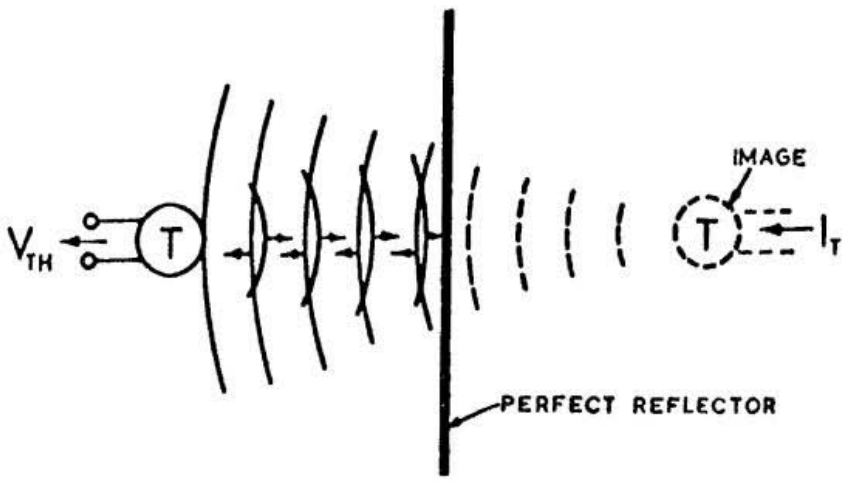

Figure 3.3: Diagram illustrating the self-reciprocity calibration measurement

computer.

3.2 Method

The principle of the self-reciprocity measurement is illustrated in Fig. 3.3 (Reid, 1974). In the self-reciprocity system a mirror reflector such as an air-water interface is used to fold the field generated by the transducer back upon the same transducer operated as a receiver. The measurement can be made either in the transducer nearfield or farfield. In the nearfield measurement the plane wave approximation is made, and in the farfield measurement a spherical wave is assumed. Pulse methods are necessary to allow time separation of the transmitted and received wave. We will use the self-reciprocity

measurement in the transducer nearfield by utilizing short pulses to calculate the absolute overall system constant and to measure echoes along the acoustical axis, as described below. Because the measurement was carried out in the transducer nearfield, the effect of beamwidth spreading will be ignored. The on-axis sound pressure received by a transducer, which acted originally as the source and is located z from air-water reflector in the nearfield is given by

$$p_s(t) = p_i R_{wa} e^{-2\alpha_w z + i\omega t} , \tag{3.1}$$

where p_i and p_s are the transmitted and received acoustic pressures. R_{wa} and α_w are the water-air reflection coefficient and attenuation in water respectively. Let $v_0(t)$ and $v_i(t)$ be, respectively, the output and input voltage of the instrument which are functions of time t, and $s_t(t)$ and $s_r(t)$ be the overall transmitting and receiving response of the system including both electronics and transducer. The instantaneous incident pressure $p_i(t)$ and instantaneous output voltage $v_0(t)$ of the receiver are respectively

$$p_i(t) = v_i(t) * s_t(t) , \tag{3.2}$$

$$v_0(t) = p_s(t) * s_r(t) , \tag{3.3}$$

where the asterisk represents the convolution operation. According to the relationship between the convolution and the Fourier Transform, we have for the frequency space

$$H_i(\omega) = V_i(\omega)S_t(\omega) \tag{3.4}$$

and

$$V_0(\omega) = H_s(\omega)S_r(\omega)\,. \tag{3.5}$$

Substituting Equations(3.2), (3.3), (3.4) , (3.5) into equation Equation(3.1), the following relationship for each frequency can be obtained

$$V_0(\omega) = V_i(\omega)S_t(\omega)S_r(\omega)R_{wa}e^{-2\alpha_w(\omega)z}$$

$$= V_i(\omega)S_M(\omega)R_{wa}e^{-2\alpha_w(\omega)z}\,, \tag{3.6}$$

In our suspension measurement we are more interested in $V_i(\omega) * S_M(\omega)$ (called overall system constant) rather than $S_M(\omega)$. In the above equation R_{wa} and $\alpha_w(\omega)$ can be calculated, while the V_0 and z are measured. So the overall system constant $S_M V_i(\omega)$ is obtained. The equation for calculating reflection coefficient R_{wa} for normal incidence is

$$R_{wa} = \frac{\rho_1 C_1 - \rho_2 C_2}{\rho_1 C_1 + \rho_2 C_2}\,, \tag{3.7}$$

where ρ_1, C_1 and ρ_2, C_2 are the density and acoustic speed in medium one and medium two respectively. In our case the R_{w-a} is around 0.9991. The attenuation of water can be calculated by (Fisher and Simmons, 1977)

$$\alpha_w = (55.9 - 2.37T + 4.77 * 10^{-2}T^2 - 3.48 * 10^{-4}T^3) * 10^{-15}f^2 , \qquad (3.8)$$

where T and f are, respectively, temperature of water and frequency. When f = 2.0 MHz and T = 20.1 ^oC, then α_w = 0.0956 m^{-1}. The data listed in Table 3.1 are the measured results for overall system constant B_c at a distance z of 10.6 cm ($B_c = \frac{V_0}{R_{w-a}} = S_M(\omega)V_t e^{-2\alpha_w z}$).

f(MHz)	1.35	1.55	1.75	1.95	2.15	2.35	2.55	2.75
$B_c(mV)$	550	800	1050	1150	1200	1100	850	650

Table 3.1: Measured sensitivity

For the reflection measurements, the distance from the source to the receiver ranged from 0.5cm to 12cm in increments of 1cm. This covers the entire nearfield for our case. To change the distance from the transducer to the water surface, water was withdrawn from the tank by siphon. The distance z between the source and the water surface was determined by the two-way travel time. For the self-reciprocity measurement, it is very important to keep the surface of the transducer parallel to the water surface.

This was done by adjusting the orientation of the transducer to get maximum output signal.

The digital oscilloscope was triggered by the 5055PR pulser/receiver for every transmission, and the amplified echo was acquired by the digital scope at a rate of 25 MHz with the reflected pulse centred in a time window 10 μs long. An FFT of 250 points with a Hann window was performed, and the average of 200 received spectra was calculated to produce an averaged spectrum. Finally the data were sent to computer to be stored for further processing. The averaged spectrum has frequency resolution of 0.2 MHz, and upper and lower 95% confidence limits are 1.097 and 0.905 respectively (Otnes and Enochson, 1972). The Hann window (Otnes and Enochson, 1972) was chosen for the FFT so leakage would be confined to frequencies close to the true frequency.

3.3 Results and Analysis

The results listed in the Table 3.1 will be discussed in Chapter 5. Figures 3.4 and 3.5 show the measurements for the relative received voltage in the transducer nearfield at 1.4, 2.0 and 2.8 MHz. In order easily to compare

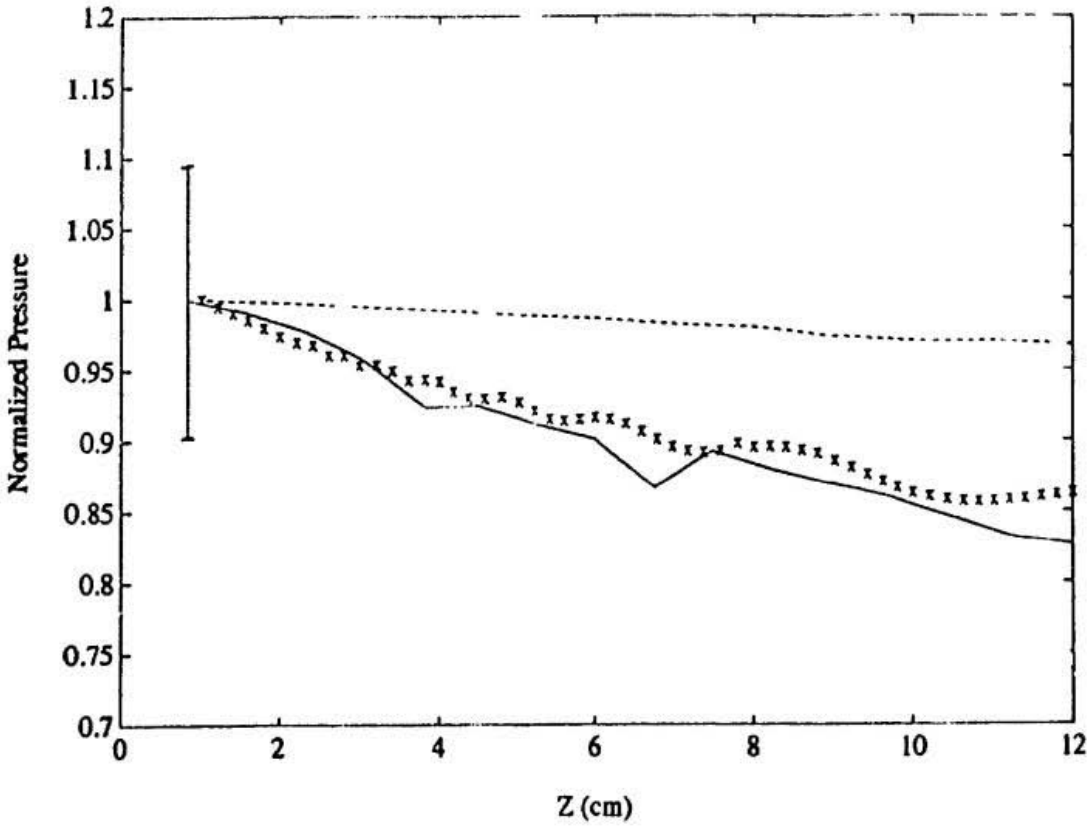

Figure 3.4: Normalized amplitudes of the pulse reflected from an air-water interface as a function of distance, at 2.0 MHz. The measurements are shown by the solid curve. The dashed and cross curves are the calculated results for a non-uniformly and uniformly vibrating piston, respectively. The error bar represents the 95% confidence limits for the measurements.

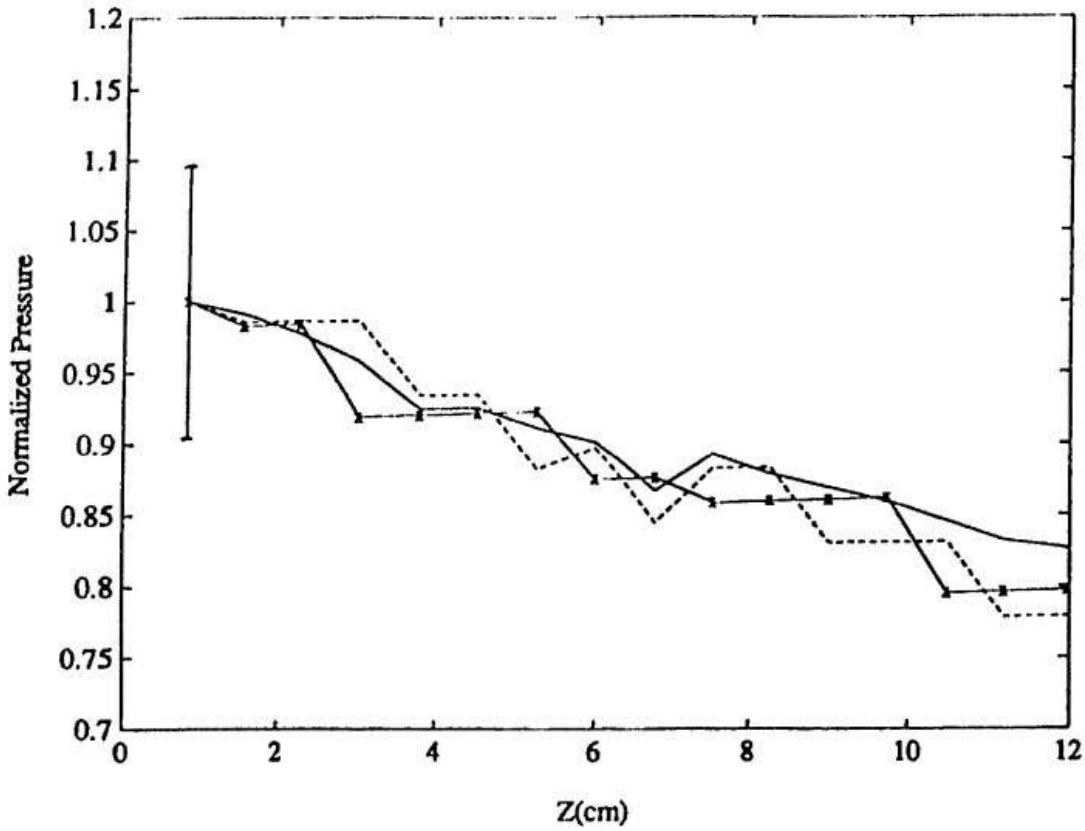

Figure 3.5: The solid, dashed, cross curve are measured voltage output of receiver against distance along acoustical axis for frequency 1.4 MHz, 2.0 MHz and 2.8 MHz, respectively.

measurements with theoretical results, in Figure 3.4 we plot them together for 2 MHz. The dashed and cross dashed curves are theoretical curves for nonuniform and uniform vibration surface respectively, which are the same as those in Figures 2.7 and 2.9 for the $\frac{a_2}{a_1} = 1$ case. The dash, solid and star curves in Figure 3.5, respectively, represent the measured results for 1.4 MHz, 2.0MHz and 2.8 MHz. We can see that the slopes of the measured curves for the three different frequencies are very similar, which means that beamwidth in the nearfield is independent of the frequency. Another interesting feature is that, comparing with the theoretical curves(cross curves) in Fig. 3.4, the measured results(solid curve) for 2.0MHz fit the theoretical curve for uniform vibration surface better than that for nonuniform vibration surface. This is discussed in detail in the next section. Although the measurement results are not as smooth as theoretical calculation, from the estimation of 95% confidence limits it can be seen that the fluctuations in the measured curves are not significant.

The Fig. 3.6 shows the magnitude of the attenuation term, $e^{-2\alpha_w(\omega)z}$, for different frequencies at the distance $z = 10.6$ cm. It can be seen that attenuation caused by water at each frequency is not very large. This correction has not been applied to the measured results in Figs. 3.4 and 3.5.

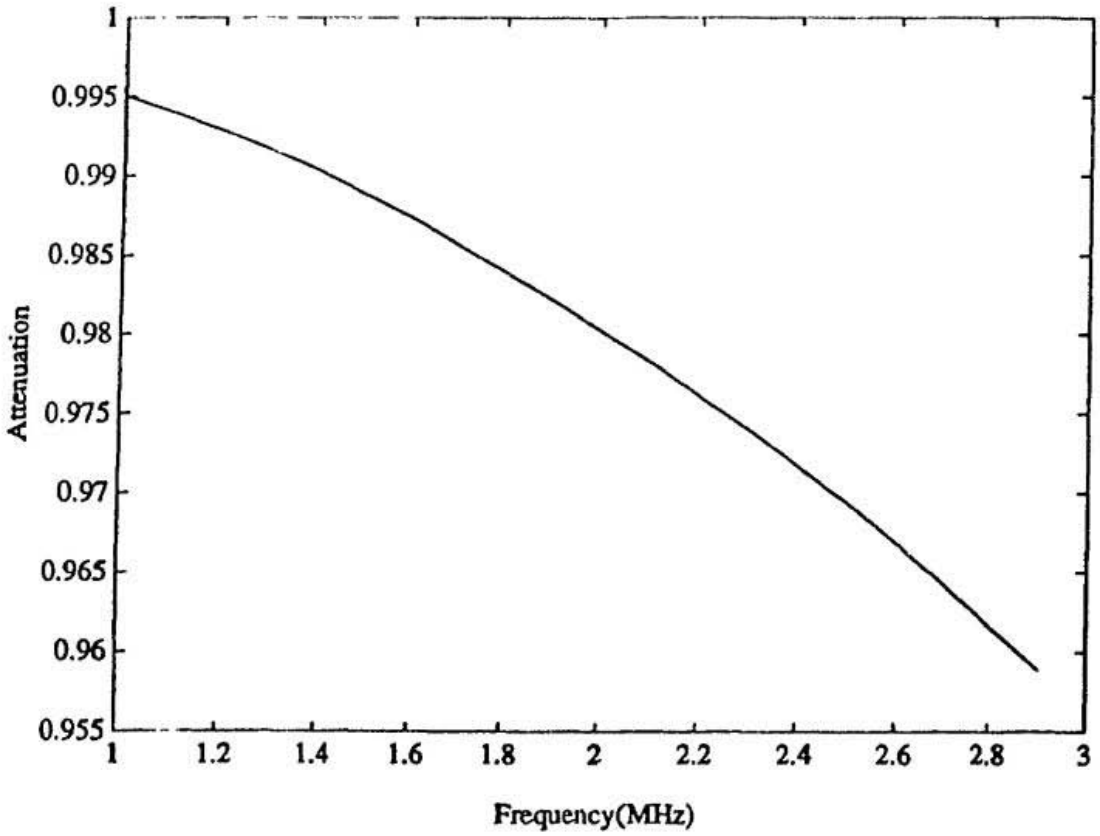

Figure 3.6: Attenuation of acoustic wave in water changes with frequency at distance 10.6 cm

3.4 The Relation of Continuous Wave Field with Transient Field

In practical applications, the pressure field for a particular frequency can be obtained either from a continuously excited transducer or from using the Fourier transform of a signal produced by a pulse excited transducer, if the pulse is long enough. That is, the pulse should be long enough that at the observation point during a pulse the wave from the nearest edge of transducer overlaps with the one coming from the farthest edge. In our case, the diameter of the transducer and the duration of the sampling time are 1.9 cm and 10 μs respectively. Here we are only interested in the nearfield which is less than 12 cm. As shown in Fig. 3.7, the distance difference between the nearest and farthest points on the transducer at 12 cm distance is given by $\Delta d = |AC - BC|$ is 0.115 cm. If the speed of sound wave in the water is taken to be 1500 m/s, during 10 μs, it will travel 1.5 cm which is much longer than Δd. This indicates that at 12 cm distance the waves coming from all parts of transducer overlap. As shown in Fig. 3.7, assuming the nearest

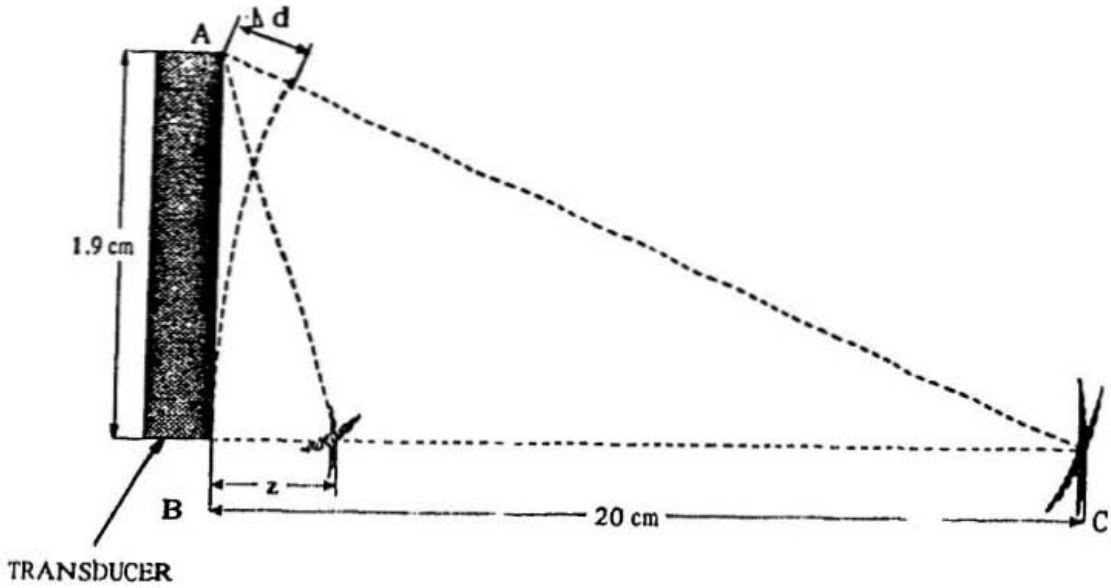

Figure 3.7: Diagram for wave path

overlapping point equal to z, it can be solved by

$$(z + 1.5)^2 = 1.9^2 + z^2 , \tag{3.9}$$

$$z = 0.45\text{cm} .$$

So waves coming from the transducer edge will overlap in the range $z > 0.45$ cm.

In the overlap region, it is easy to obtain the relationship between the pulse produced field and the continuous wave field. Letting $v_0(\rho_1, o_1, t)$ and $h(R, t)$ be velocity distribution on the surface of the transducer and impulse response respectively, the velocity potential at the field point is their convo-

lution in the time domain (refer to Fig. 2.2 for coordinate system), i.e.

$$\phi(R,t) = \int\int_{S_1} v_0(\rho_1,\phi_1,t) * h(R,t)ds_1 . \qquad (3.10)$$

For a point source, the impulse response can be expressed as $h(R,t) = \frac{\delta(t-\frac{R}{c})}{2\pi R}$. According to the relation between convolution and Fourier transform, in the frequency domain the velocity potential can be written as a product of the transforms of the two time functions, i.e.

$$\Phi(R,\omega) = \int\int_{S} \Psi(\rho_1,\phi_1,\omega)\frac{e^{-i\omega R/c}}{2\pi R}ds , \qquad (3.11)$$

where $\Phi(R,\omega)$, $\Psi(\rho_1,\phi_1,\omega)$, and $\frac{e^{-i\omega R/c}}{2\pi R}$ are the Fourier transforms of velocity potential, piston velocity, and impulse response respectively.

Equation (3.11) is the Rayleigh surface integral and has the same form as equation (2.24) for the continuous wave case except $\Psi(\rho,\phi_1,\omega)$, is now a function of frequency. In Chapter 2, the transducer nearfield calculated is produced by single frequency vibration source at the first vibrational mode which is more like the case of narrowband transducer. Usually a narrowband transducer is designed to work at the resonant frequency of the lowest vibrating mode, which is determined by the thickness of the crystal, to produce the largest possible transmitting energy. However, for the pulse excited broadband piston, in addition to the lowest order resonant vibrating mode, the

higher order resonant or other modes also affect the acoustical pressure field. So the surface vibration of a broadband transducer should be expressed by equation 2.20. In order to get a better approximation for the first vibrational mode, a larger number of terms in the equation 2.20 should be counted, which means that there are more than one velocity distribution mode on transducer surface to contribute acoustical field for same frequency.

Chapter 4

BACKSCATTER FROM SUSPENSIONS

In this chapter, relationships are derived between the output voltage of the receiver, and the size, concentration, and backscattering cross section of suspended grains. We begin with a discussion of scattering from a single spherical particle. The rigid movable sphere model is used, then, to consider scattering from an ensemble of particles in the detected volume. Here, multiple scattering effects will be ignored because we only consider the low concentration case.

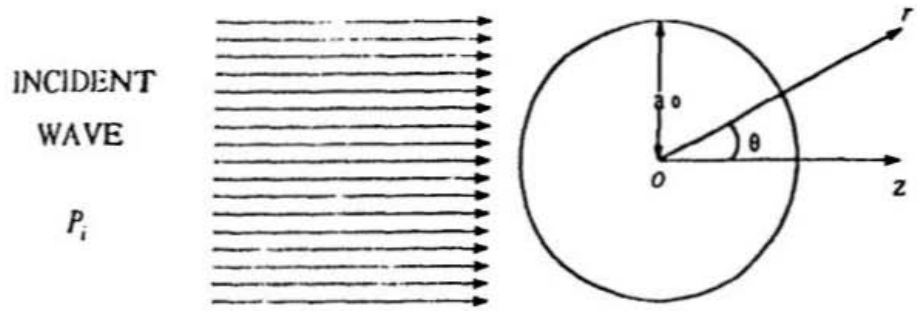

Figure 4.1: A plane wave backscattered by a rigid sphere

4.1 Backscattered Pressure from a Single Particle

We first consider the backscattered acoustic field from a movable rigid sphere as shown in fig. 4.1. A plane wave coming from the negative z direction can be expressed as

$$p_i = p_a e^{i(\omega t - kz)} . \tag{4.1}$$

Referring to Faran (1951), Hickling (1962) and Hay and Mercer (1985), the wave scattered by a rigid sphere is expressed as a sum of partial scattered waves. At points many wavelengths from the center of the scatterer, the amplitude of the scattered wave takes the form

$$p_s = \frac{p_i a_0 f_\infty(\theta, x)}{2r} . \tag{4.2}$$

Here a_0 is the radius of the sphere, $x = ka_0$ is the size frequency parameter, and $f_\infty(x, \theta)$ is the form factor given by

$$f_\infty(\theta, x) = -\frac{2}{x}\sum_{n=0}^{\infty}(2n+1)\sin\delta_n e^{i\delta_n}P_n(\cos\theta), \tag{4.3}$$

where δ_n is the phase shift of the n-th partial wave. For $\theta = 180°$, the backscattering case,

$$f_\infty(x) = -\frac{2}{x}\sum_{n=0}^{\infty}(2n+1)(-1)^n\sin\delta_n e^{i\delta_n}. \tag{4.4}$$

When the incident wave is a pulse, which may be regarded as a function of time, the incident and scattered pressure pulses have frequency spectra $H_i(\omega)$ and $H_s(\omega)$, respectively, whose instantaneous time history in t is expressed according to the Fourier theorem by the integral

$$p_i(t) = \int_{-\infty}^{\infty} H_i(\omega)e^{i\omega t}d\omega \tag{4.5}$$

and

$$p_s(t) = \int_{-\infty}^{\infty} H_s(\omega)e^{i\omega t}d\omega. \tag{4.6}$$

The inverse transform defining the pulse spectrum is

$$H_i(\omega) = \frac{1}{2\pi}\int_{-\infty}^{\infty} p_i(t)e^{-i\omega t}dt \tag{4.7}$$

and

$$\Pi_s(\omega) = \frac{1}{2\pi}\int_{-\infty}^{\infty} p_s(t)e^{-i\omega t}dt\,. \tag{4.8}$$

The quantities $p_i(t)$ and $p_s(t)$ are now instantaneous pressures in the equation (4.2), and the relationship between them, in terms of $|\,f_\infty(x)\,|$, is (integrating both sides of equation (4.2) with time)

$$\int_{-\infty}^{\infty} p_s(t)e^{-i\omega t}dt = \frac{a_0}{2z}f_\infty(x)\int_{-\infty}^{\infty} p_i(t)e^{-i\omega t}dt\,, \tag{4.9}$$

or further

$$\begin{aligned} |\,f_\infty(x)\,| &= \frac{2z}{a_0}\frac{|\int_{-\infty}^{\infty} p_s(t)e^{-i\omega t}dt\,|}{|\int_{-\infty}^{\infty} p_i(t)e^{-i\omega t}dt\,|} \\ &= \frac{2z}{a_0}\frac{|\,\Pi_s(\omega)\,|}{|\,\Pi_i(\omega)\,|}\,. \end{aligned} \tag{4.10}$$

Substituting equation (3.4) and equation (3.5) into equation (4.10), the output voltage of one frequency component of the backscatter from a movable rigid sphere is

$$V_0(\omega) = \frac{S_r(\omega)S_t(\omega)V_i(\omega)a_0\,|\,f_\infty(x)\,|}{2z}\,. \tag{4.11}$$

4.2 Backscattered Pressure From An Ensemble Of Particles

Now consider the backscattered signal from a cloud of scatterers where we use the subscript j to refer to different particles. In our application, multiple scattering effects are ignored because the data used were all acquired at concentrations less than 10 kg m^{-3} in which range the data do exhibit that multiple scattering is not important (Varadan et al. 1985, Hay 1991). The total scattered pressure from all scatterers in the ensemble depends on whether a pulsed or continous wave detection system is used (Hay, 1983). For a continuous wave detection system, because the relative positions of the scatterers within the detected volume change randomly with time, the scattered waves are incoherent and the total intensity of a backscattered radiation field produced by uniformly distributed, noninteracting scatterers (i.e. no multiple scattering), can be expressed by

$$I_0(\omega) = \sum_j V_{0j}(\omega) V_{0j}^*(\omega) \,, \tag{4.12}$$

where V_{oj}^* is the complex conjugate of V_{oj}.

For typical pulsed detection systems, however, the duration of the trans-

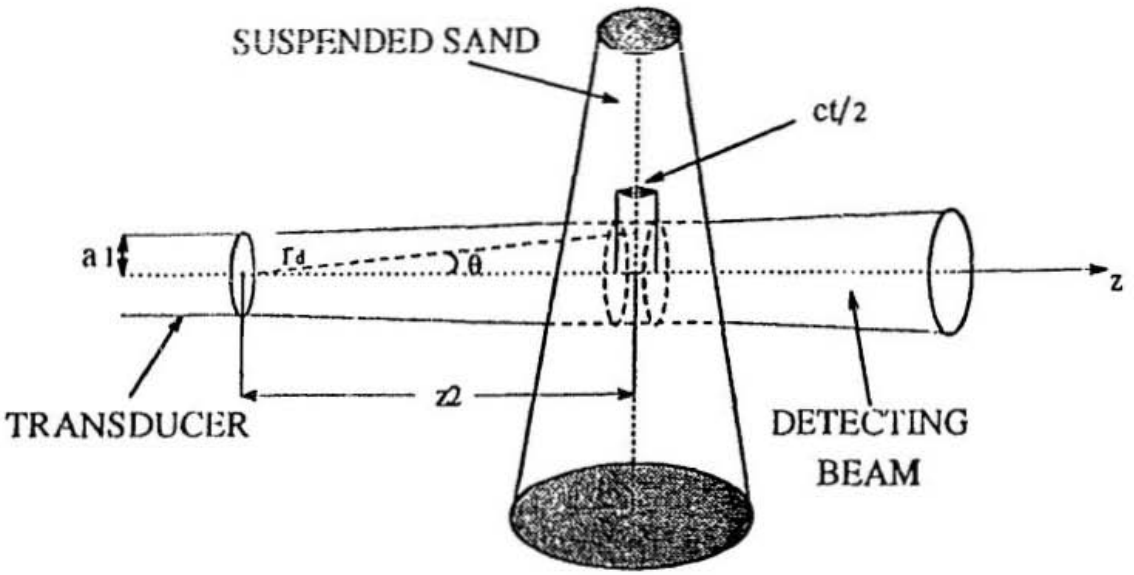

Figure 4.2: Geometry of suspended sand measurement

mitted pulse is usually much less than the time required for the scatterers to change relative position by an acoustic wavelength, so that the scattered waves from a single pulse are coherent. From pulse to pulse, however, the scattered waves are normally incoherent. This means that the signal amplitude is Rayleigh-distributed from pulse to pulse, and it has been shown (Hay, 1983) that the pulse-to-pulse backscattered intensity is given by

$$I_0(\omega) = \frac{\pi}{4} \sum_j V_{0j}(\omega) V_{0j}^*(\omega) , \qquad (4.13)$$

Let N be the number of particles per unit volume, α be the absorption coefficient of water, and $V_d(\theta, z)$ be the detected volume. From Fig. 4.2 it is easy to show that

$$dV_d = 2\pi z tan\theta \frac{z}{cos\theta} d\theta dz$$
$$= \frac{2\pi tan\theta z^2}{cos\theta} d\theta dz$$

If the detected volume is not large (detected volume in our measurement system is around 2.1 cm^3), the concentration of sand in it can be considered to be uniform. From equation(4.11), (4.13) and considering effect of the directivity $D(\theta, \omega)$ of the transducer, we have the square of the detected voltage for a cloud of scatterers

$$I_0(\omega) = \frac{\pi}{4} \int\int\int_V \frac{S_M^2(\omega) D^4(\theta,\omega) a_0^2 \mid V_i(\omega) \mid^2 \mid f_\infty(x) \mid^2}{4z^2} e^{-4\alpha_w(\omega)z} N dV_d ,$$
$$= \frac{\pi S_M^2(\omega) a_0^2 \mid V_i(\omega) \mid^2 \mid f_\infty(x) \mid^2}{16} \int_{z_2 - \frac{C\tau}{4}}^{z_2 + \frac{C\tau}{4}} \frac{1}{z^2}$$
$$[\int_0^{cos^{-1}\frac{s}{r_d}} D^4(\theta,\omega) \frac{2\pi tan\theta}{cos\theta} z^2 d\theta] e^{-4\alpha_w(\omega)z} N dz , \qquad (4.14)$$

where τ and C are the duration of the sampling window and the acoustical wave speed in the liquid in which the sand is suspended, and $S_M = S_{r_2} S_t$. The integration in square bracket represents effects of directivity on the whole detected cross section. From the theoretical calculations in Chapter 2 and

the measurements in Chapter 3, we know that although acoustical pressures in the nearfield for different points are very different, the average pressure across the beam changes usually by less than 10 %. So it may be reasonable to assume that averaged directivity in the nearfield can be considered as the constant $\overline{D(\omega)}$ multiplied by a function $G(z)$ of average acoustical pressure density, which decreases as z increases because beamwidth spreading with distance from the transducer. Assume A is the area of transducer surface, then equation (4.14) can be then rewritten as

$$I_0(\omega) = S_M^2 \frac{\overline{D^4(\omega)} N A \pi a_0^2 \mid V_i(\omega) \mid^2 \mid f_\infty(x) \mid^2}{16} \int_{z_2-\frac{cT}{4}}^{z_2+\frac{cT}{4}} \frac{G(z) e^{-4\alpha_w z}}{z^2} dz \quad (4.15)$$

Usually, we measure the mass concentration, M, of suspended particles instead of the number of particles, N, per unit volume. The relation between M and N can be expressed by

$$M = N \frac{4}{3} \pi a_0^3 \rho \,, \quad (4.16)$$

where ρ is the bulk density of the suspended sand. Then we have

$$I(\omega) = \frac{\overline{D^4(\omega)} 3 M A \mid V_i(\omega) \mid^2 \mid f_\infty(x) \mid^2}{64 \rho a_0} \mid S_M(\omega) \mid^2 \int_{z_2-\frac{cT}{4}}^{z_2+\frac{cT}{4}} \frac{G(z) e^{-4\alpha_w z}}{z^2} dz \,. \quad (4.17)$$

Letting

$$B(z,\omega) = \sqrt{\frac{3S_M^2\overline{D^4}\mid V_i(\omega)\mid^2 Ak}{64\rho}\int_{z-\frac{r}{4}}^{z+\frac{r}{4}}\frac{\overline{G(z,\omega-\omega_0)}}{z^2}dz} \qquad (4.18)$$

the output voltage due to the backscattered signal becomes

$$V_0(\omega) = B(z,\omega)\sqrt{\frac{M}{x}}\mid f_\infty(x)\mid . \qquad (4.19)$$

This relation shows that the output voltage of the backscattered signal is affected by both concentration and size of the suspended sand, and the square of output voltage $\mid V_0 \mid^2$ is proportional to the mass concentration M.

Chapter 5

MEASUREMENT OF FORM FACTOR IN THE LABORATORY

5.1 Experimental Design And Method Description

The form factor measurements were carried out in the tank with circulation system which is shown in Fig. 5.1, and is discussed in detail by Hay

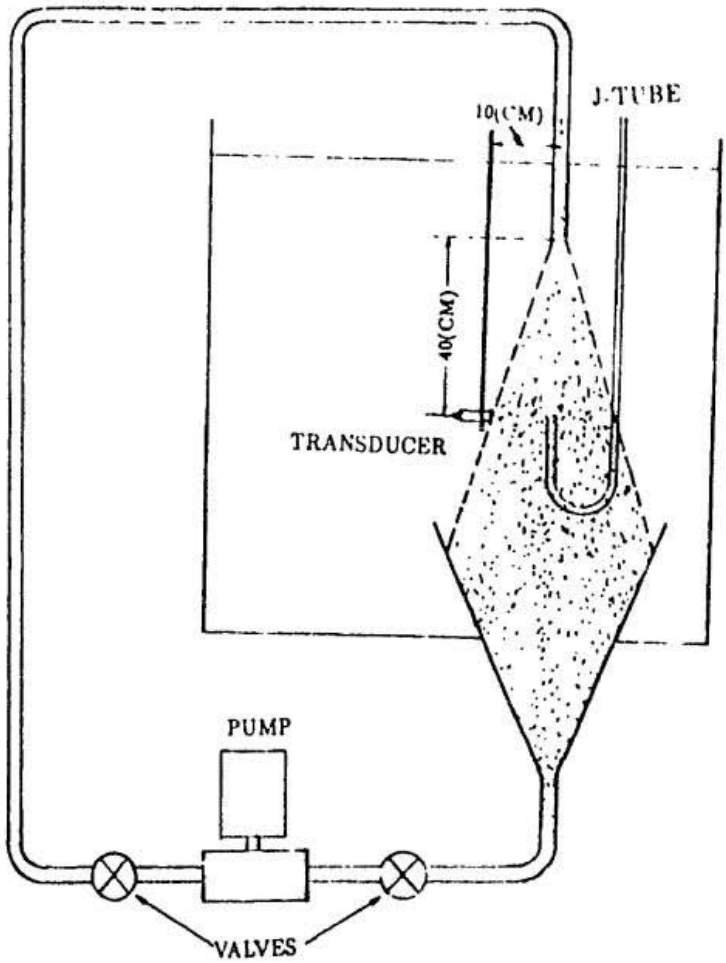

Figure 5.1: Sketch of experimental set up. Shading indicates suspended sediment jet, and sediment cloud in capture cone

(1991). The suspended sediment jet is driven by a pump, and the jet velocity is controlled by a throttling section in the discharge line. At the base of the tank, the jet enters a receiving cone of circular cross-section with an inlet diameter of 56 cm. The vertical distance from the jet orifice to the centerline of the transducer was 40 cm. The diameter of suspended sand cloud at the level

sized fractions (μm)	midpoint size $2a_0(\mu m)$	x -ka_0 (at 2.0MHz)
106 - 125	116	0.486
125 - 150	137	0.574
150 - 180	165	0.691
180 - 212	196	0.821
212 - 250	231	0.968
250 - 300	275	1.150
300 - 355	327	1.370
355 - 425	390	1.634

Table 5.1: Sized fraction of beach sand used for form factor measurements

of the transducer was estimated to be about 10 cm. The surface of the transducer was 10.6 cm away from the jet centerline which was therefore in the nearfield. The J-tube was used for syphoning suspended sediment samples for concentration determination. Through adjusting the transducer direction vertically and horizontally by getting the maximum reflection signal from a wire suspended through the centre of the discharge nozzle, we can align the transducer to make its axis intersect the jet's centerline perpendicularly. Tap water was used in our experiment.

The sand used in the experiment was beach sand, and was mechanically sieved into a few differently sized fractions listed in Table 5.1 . To determine the absolute concentration, water samples from the jet flow were taken after each backscatter run using the J- tube. Then, the sample volume was mea-

sured and, being dried, the sand particles were weighed. By calculating the ratio of the weight of the dried sand to the volume of the mixture, the sample concentration was determined. For better accuracy, four suction samples were taken; standard error as a percentage of the mean of the four samples in our experiments ranged from 0.24 % to 4.45 %.

The concentration distribution across the jet is Gaussian (Hay, 1991), and can be expressed by

$$C(z - z_2) = C_0 e^{\frac{-(z-z_2)^2}{2\sigma^2}} \qquad (5.1)$$

where z is the horizontal coordinate, and z_2 is the distance from transducer to the centerline of the jet. C_0 is the sand concentration at the centerline of the jet. The standard deviation, σ, changes with the sand size. For our case $\sigma \approx 2.8$ cm. The position where the concentration decreases 5% relative to the concentration at $z = z_2$ is determined by solving

$$0.95 = e^{\frac{-(z-z_2)^2}{2(2.8)^2}} . \qquad (5.2)$$

Thus,

$$(z - z_2) = \mid \sqrt{-15.68 ln 0.95} \mid \approx 0.9\text{cm}$$

It should therefore be reasonable to assume that for our measurement width of 0.75 cm, the concentration of suspended sand is uniform.

The apparatus for measuring the form function and their settings are almost the same as in Chapter 3. However, a difference exists in the receiving attenuation selection (40dB difference) of the 5055PR pulser/receiver. This is because the backscattering signal from suspended sand is much smaller than the reflection signal from the water-air interface. As in Chapter 3, the backscattered signal of 10 μs duration was digitized at a rate of 25 MHz, and a 250 point FFT with Hann window performed in the function memory of digital oscilloscope to produce spectra with 0.2 MHz frequency resolution. Because the distribution of sand is random and the turbulance in the jet circulation produces fluctuations in concentration, the fluctuations in the backscattered signal were large. In order to obtain a stable backscattered spectrum, we averaged the spectra from 200 pulses. Each run lasted 1.50 minutes.

5.2 Backscattered Amplitudes Versus Particle Mass Concentration

Equation (4.19) tells us that output voltage, V_0, of the receiver is

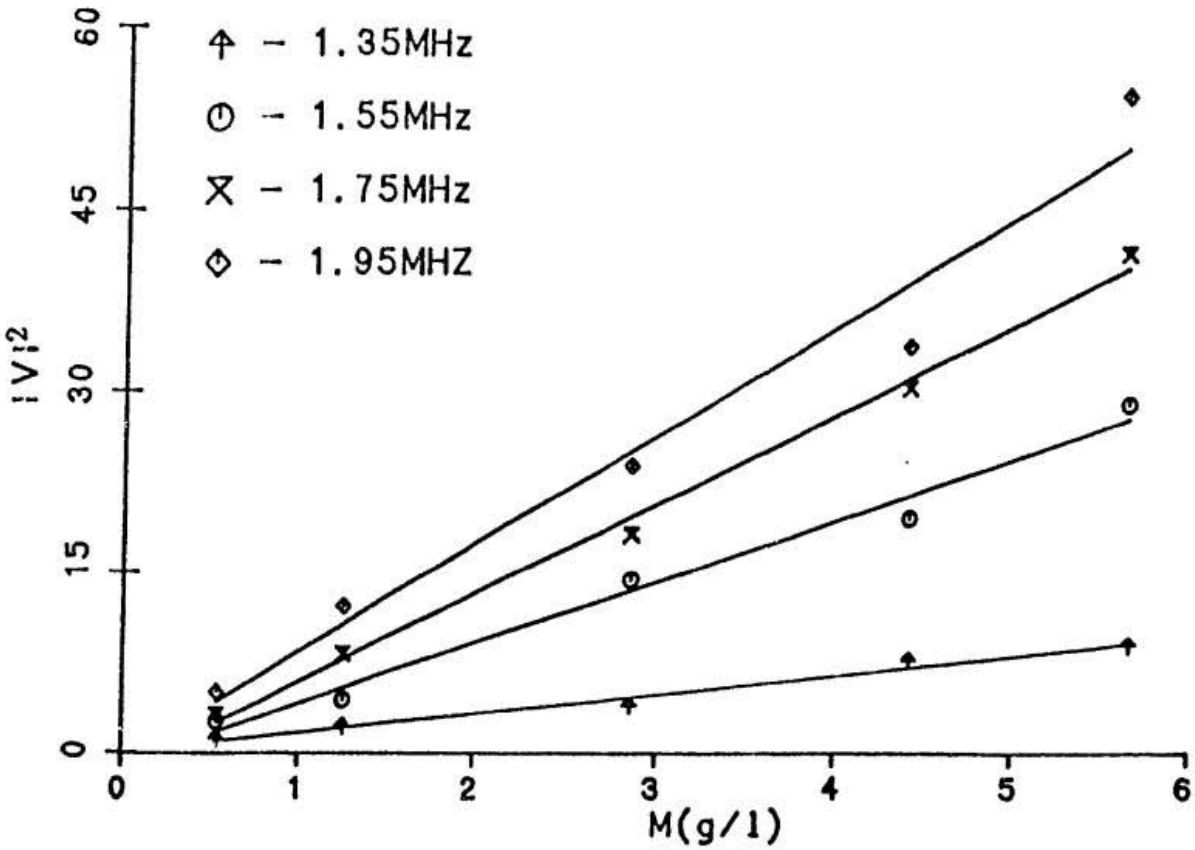

Figure 5.2: Squared-mean backscatter(in Volt^2) as a function of beach sand concentration at 1.35 MHz to 1.95 MHz. Straight lines were obtained by least squares fit to all measured points. Different symbols represent different frequencies, as shown.

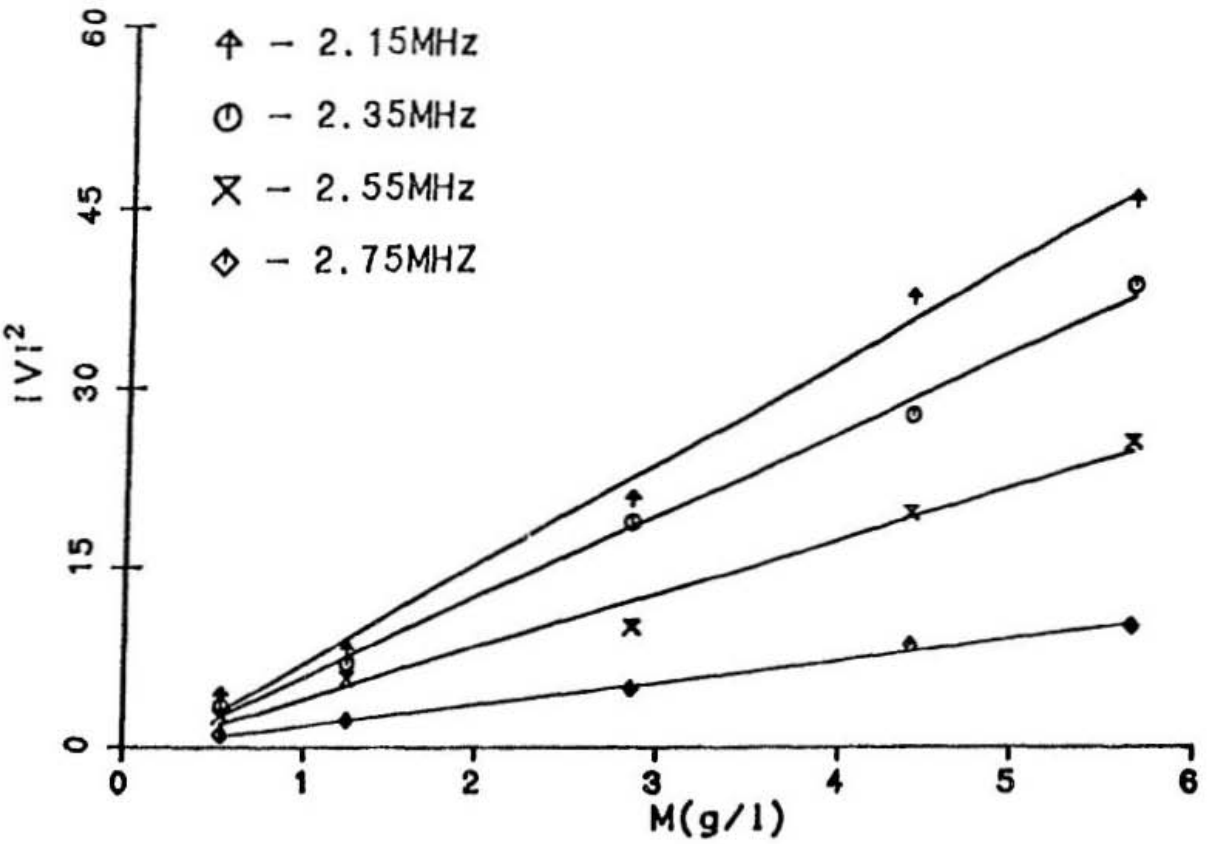

Figure 5.3: Squared-mean backscatter(in Volt^2) as a function of beach sand concentration at 2.15 MHz to 2.75 MHz. Straight lines were obtained by least squares fit to all measured points. Different symbols represent different frequencies, as shown.

proportional to the square root of the mass concentration M. Figures 5.2 and 5.3 show the measurement results at frequencies from 1.35 MHz to 2.75 MHz, which were obtained by measuring beach sand of 180-212 diameter with 5 different concentrations. In the figures, the symbols represent measurement results which are averaged 200 times, and the solid line is the least-squares fit. It can be seen that the measurements are reasonably linear at all frequencies. This is evidence that, in the absence of multiple scattering, the mean squared backscattering signal should be linearly proportional to particle concentration which has been reported by far field measurements (Hay, 1991)

5.3 Estimation of System Constant

The measurement of the form factor in the far acoustical pressure field by using a narrow-band transducer has been made by Hay (1991). The results show that for the rigid movable spherical model, the measurements made in the laboratory fit the theoretical curve reasonably well. Our idea for measuring the system constant is to assume that, in the nearfield, the form factor calculated from the rigid movable spherical model will fit the form factor measured by the broadband transducer. Then we can use a known

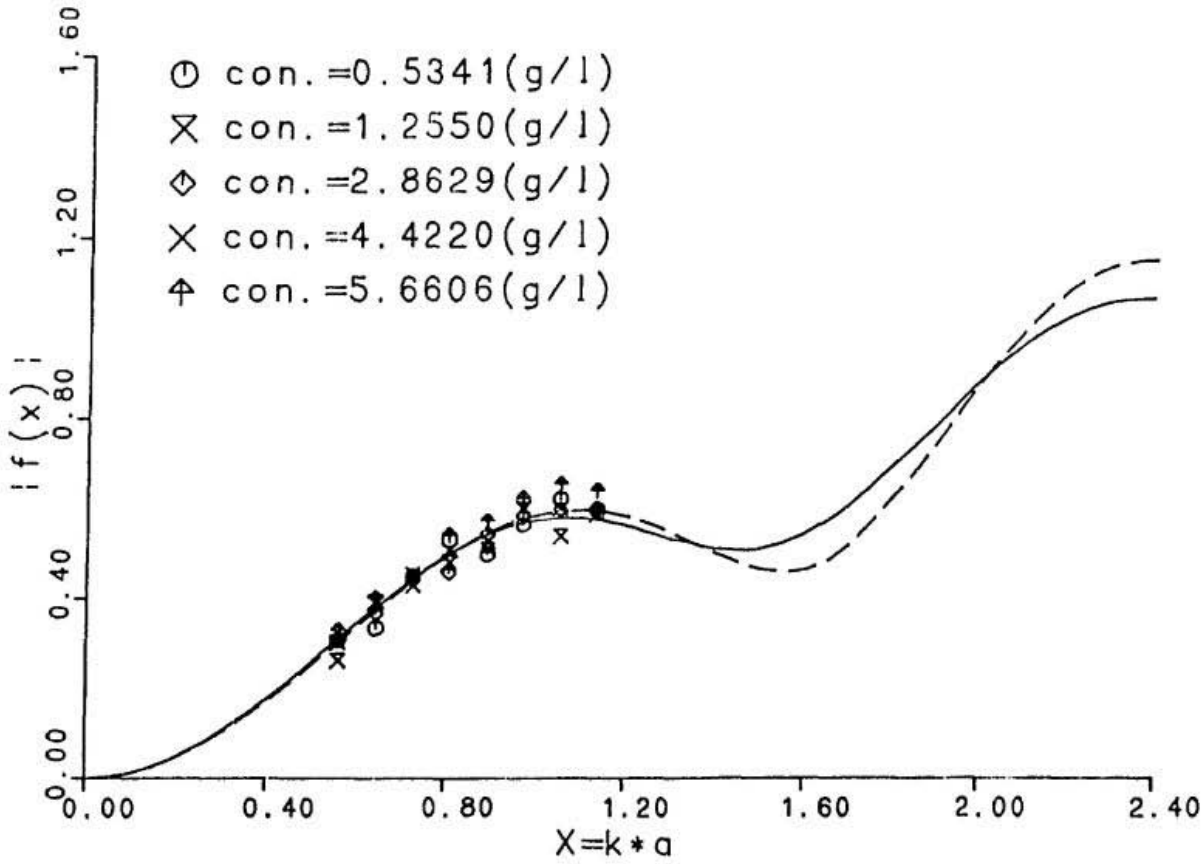

Figure 5.4: Backscatter form factor $| f_\infty(x) |$ for 180-212 μm diameter beach sand. Different symbols represent different concentrations, as shown.

size and concentration of sand and from equation (4.19) the overall system constant B is obtained.

Figure 5.4 shows the results using the data in Figures 5.2 to 5.3. The dashed line is the theoretical form factor $| f_\infty(x) |$ for a rigid sphere calculated from equation 4.4. In our application the sand size we measured has a narrow band instead of being a single size (see Table 5.1), with the same being true for the frequency (Δf = 0.2MHz). The backscattered signals

f(MHz)	1.35	1.55	1.75	1.95	2.15	2.35	2.55	2.75
$\overline{B}(mV/(kg/m^3)^{1/2}$	3.4	4.7	5.3	5.7	5.3	4.6	3.8	2.6
$B_m(mV/(kg/m^3)^{1/2}$	2.4	3.7	5.2	6.0	6.5	6.2	5.0	3.9
$\overline{B}/B_m$	1.42	1.27	1.02	0.95	0.82	0.74	0.76	0.67

Table 5.2: Averaged overall system constant $\overline{B}$, determined by least squares to backscatter measurements and B_m determined from reflection measurements.

include all contributions from different sizes and frequencies in these narrow bands. So it should be more reasonable to fit the measured results using a smoothed theoretical form factor of the rigid spherical model. We did the smoothing by finding range of x ($\Delta x = \Delta k a_0 + k\Delta a_0$) from sand size and frequency bandwidth, and averaged the theoretical form factor of a rigid sphere within Δx. The solid curve in Fig. 5.4 is the smoothed results, and it can be seen in later Figures that the smoothed curve fits the measurements better than the unsmoothed one. We force the measured values to fit the smoothed theoretical form factor curve. For a given frequency and particle size an average B, denoted by $\overline{B}$, may be obtained using equation (4.19) for measurements of $V_0(\omega)$ made at different concentrations. The resulting values of $\overline{B}$ for different frequencies at a distance of 10.6 cm from the receiver surface are listed in Table 5.2.

The overall system constant B can also be calculated from the data for B_c (see Table 3.1), obtained from the air-water surface reflection measurements. Using the expression (4.18), we assume that $G(z)$ and z are constant, denoted as $G_0(z_2)$ and $z = z_2$, in the detected volume because in our case they do not change much. The expression (4.18) will be simplified as

$$B_m(z_2,\omega) = \overline{D^2(\omega)} \mid V_i(\omega) \mid S_M(\omega) e^{-2\alpha_w z_2} \sqrt{\frac{3kAC\tau G_0(z_2)}{128\rho z_2^2}}$$

$$= B_c \sqrt{\frac{3kAC\tau}{128\rho z_2^2}} \qquad (5.3)$$

The values of B_m listed in Table 5.2 are the calculated results for $G_0(z_2) = 1$, $A = 2.85$ cm^2, $\rho = 2700$ kg m^{-3}, $C = 1496$ m s^{-1}, $\tau = 10\mu$s and $z_2 = 10.6$ cm.

Comparing $\overline{B}$ with B_m, we find that at frequencies near the centre frequency of 2MHz agreement is reasonably good. However, at low and high frequencies the differences between them are as large as 30 to 40 %. One possible explanation for the discrepancy is that in the form factor measurement the suspended particles occupy most of the space between the transducer and the detected volume. When an acoustical wave travels between the transducer and the detected volume, its energy will be attenuated by scattering from the particles. This attenuation increases with increasing frequency.

The overall system constant $\overline{B}$ obtained by measuring beach sand therefore could be smaller than B_m measured by reflection from the air-water interface at high frequencies , as indicated in Table 5.2, because the additional attenuation due to particles is present. So correction for the additional attenuation at high frequency region should be considered in order to improve measurement. At lower frequencies attenuation is unimportant. The beam width spreading, indicated by the drop in the reflected signal amplitudes with distance in fig. 3.5, suggests that the cross-section area of the detected volume for suspended sand measurement should be larger than A, the area of the transducer, which was used for calculation of B_m in equation 5.3. This could be reason to cause $B_m < \overline{B}$ at low frequencies. Other possibilities are that: (1) the signal to noise ratio decreases for frequency components away from the centre frequency; (2) the receiving gain of pulser/receiver used for the reflection and scattering measurements was not the same (40dB difference); (3) it is hard to know the exact detected volume and directivity of the transducer at each frequency, the overall system constant B_m calculated from equation 5.3 is not very accurate. So the overall system constant $\overline{B}$ obtained from measuring suspended particles is believed to be more realistic

T=20.9 °C				C (m/s) = 1484.4			
size(μm)	$2a_0(\mu m)$	concentration(g/l)					
106-125	115.5	0.3550	0.9974	2.0219	3.3247	4.0941	4.6652
180-212	196.0	0.5539	1.1524	2.1342	3.1236	4.2719	5.2654
300-350	325.0	0.4181	1.1445	1.9942	2.4636	3.0097	3.7499

Table 5.3: T - temperature, C - acoustic speed in water, a_0 - radius of middle size

and reliable than B_m.

5.4 Measurement Of The Form Factor

The overall averaged constant $\overline{B}$ for different frequencies was estimated in the last section from acoustical signals backscattered from particles of the same size, but different concentrations, by fitting to the theoretical curve of the form function. The range of $x(= ka)$ considered in obtaining the overall constant B is from 0.56 to 1.1. If $\overline{B}$ is correct, the measured curve of the form function should fit the theoretical calculation reasonably well for a wider range of x.

Three sets of experiments were carried out using different sizes and concentrations which are listed in Table 5.3, and the results are shown in Figures 5.5 to 5.7 as $\mid f_\infty(x) \mid$ plotted against x, where a, in this case, is taken

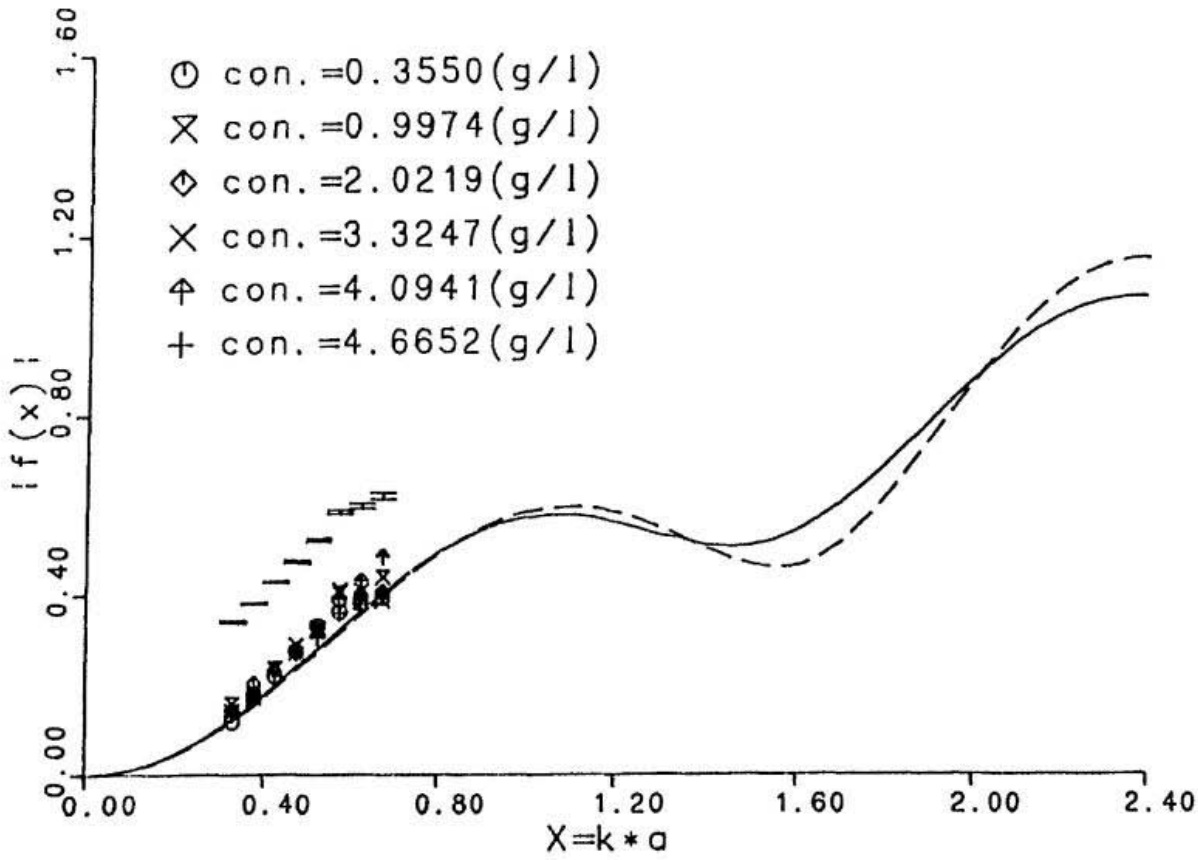

Figure 5.5: Backscatter form factor $| f_\infty(x) |$ for 106-125 μm diameter beach sand

to be the midpoint of the $\frac{1}{4}$-phi sieve interval. The measurements cover the range of x from 0.33 to 1.9 and include sand sizes of 115.5μm, 196μm and 327.5μm at frequencies ranging from 1.35 MHz to 2.75 MHz. For each sand size, measurements were taken at six different concentrations. The overall averaged constant $\overline{B}$ obtained in the last section was used for calculating $| f_\infty(x) |$ from the measurements. To check repeatability, further measurements were made using suspended sand of the same size as that in Fig. 5.4

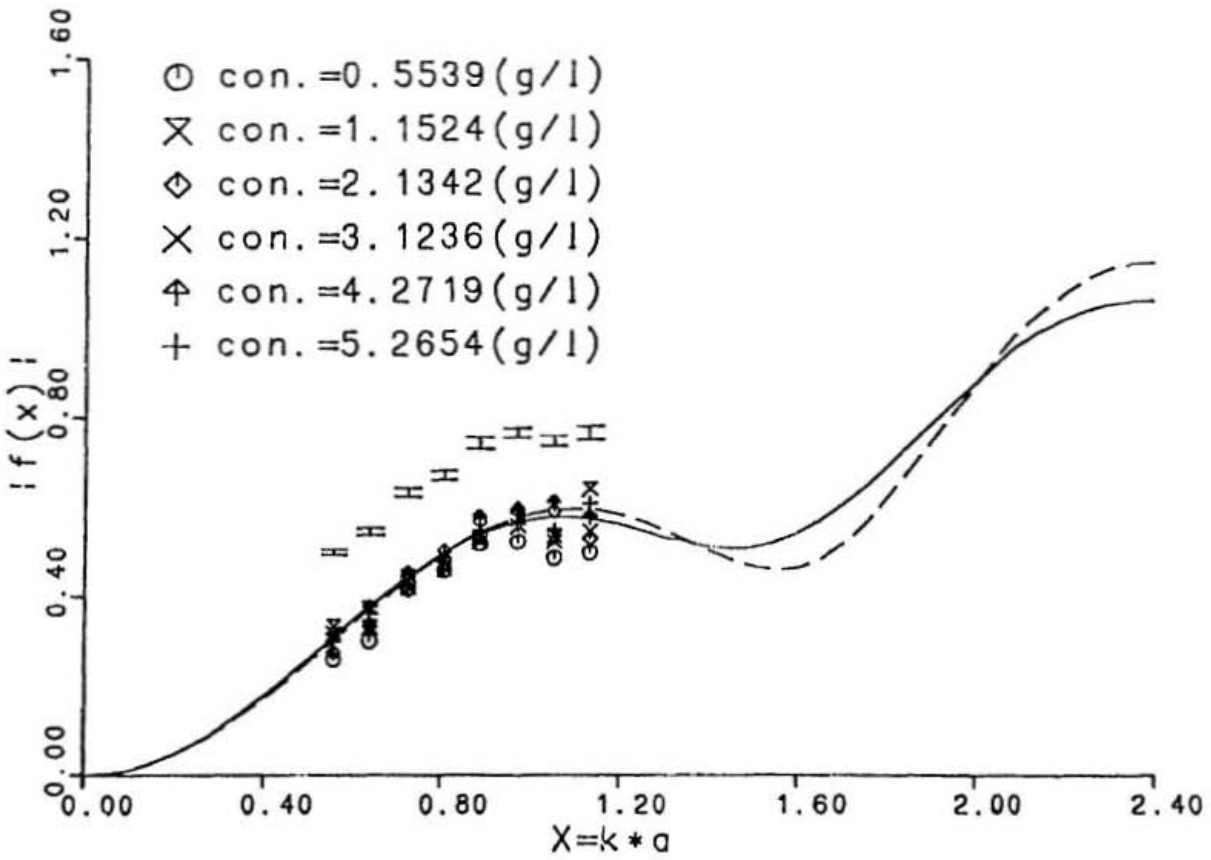

Figure 5.6: Backscatter form factor | $f_\infty(x)$ | for 180-212 μm diameter beach sand

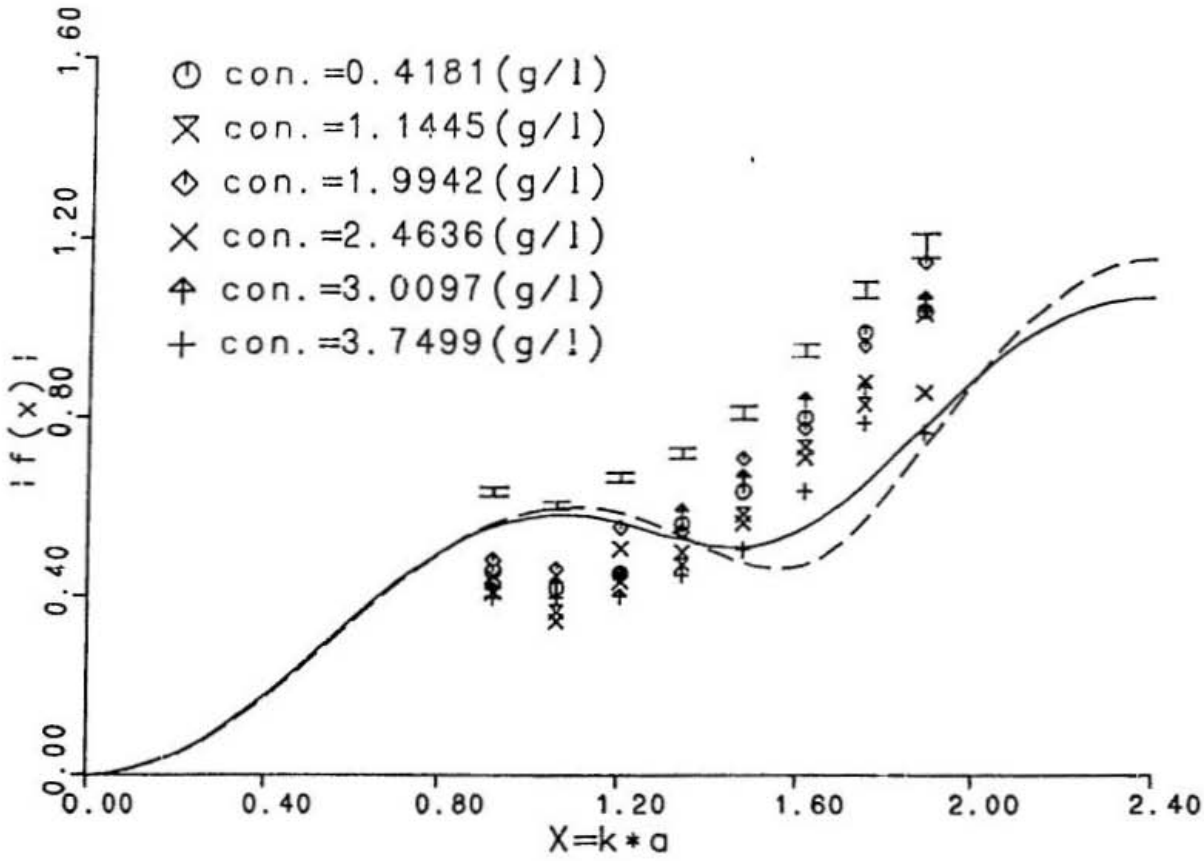

Figure 5.7: Backscatter form factor | $f_\infty(x)$ | for 300-350 μm diameter beach sand

f(MHz)	1.35	1.55	1.75	1.95	2.15	2.35	2.55	2.75
$\Delta B(\%)$	3.24	2.76	1.88	2.62	2.22	1.40	2.61	1.47
$\Delta\frac{V_0}{\sqrt{M}}(\%)(106-125\mu m)$	4.73	3.56	2.19	2.77	2.46	2.47	3.16	3.51
$\Delta\frac{V_0}{\sqrt{M}}(\%)(180-212\mu m)$	3.35	3.05	1.29	1.34	1.71	1.72	3.10	3.41
$\Delta\frac{V_0}{\sqrt{M}}(\%)(300-350\mu m)$	4.55	4.77	4.72	4.50	1.93	3.79	4.10	5.52

Table 5.4: The list of standard errors as percentage of mean of the samples

($196\mu m$) but at different concentration. The result is shown in the Fig. 5.6. It can be seen that the two different sets of measured values are similar.

The precision of these form factor estimates was determined as follows. From equation (4.19) it can be seen that the error in the experimental value of $\mid f_\infty \mid$ is due to the error in the system constant B and in the ratio of $\frac{V_0}{\sqrt{M}}$. The standard errors in the values of B were estimated from the five separate determinations for each frequency (see Fig. 5.4), and are listed as percentages of the mean Table 5.4. Similarly, the standard errors in $\frac{V_0}{\sqrt{M}}$ were estimated from the 6 measurements at each frequency (see Table 5.3) and are also listed in Table 5.4. The standard error in $\mid f_\infty \mid$ was taken to be $[(\Delta B\%)^2 + (\Delta\frac{V_0}{\sqrt{M}}\%)^2]^{\frac{1}{2}}$, and is represented by the error bars in Figures 5.5 to 5.7.

In order to easily compare with the theoretical curve, we combine the data

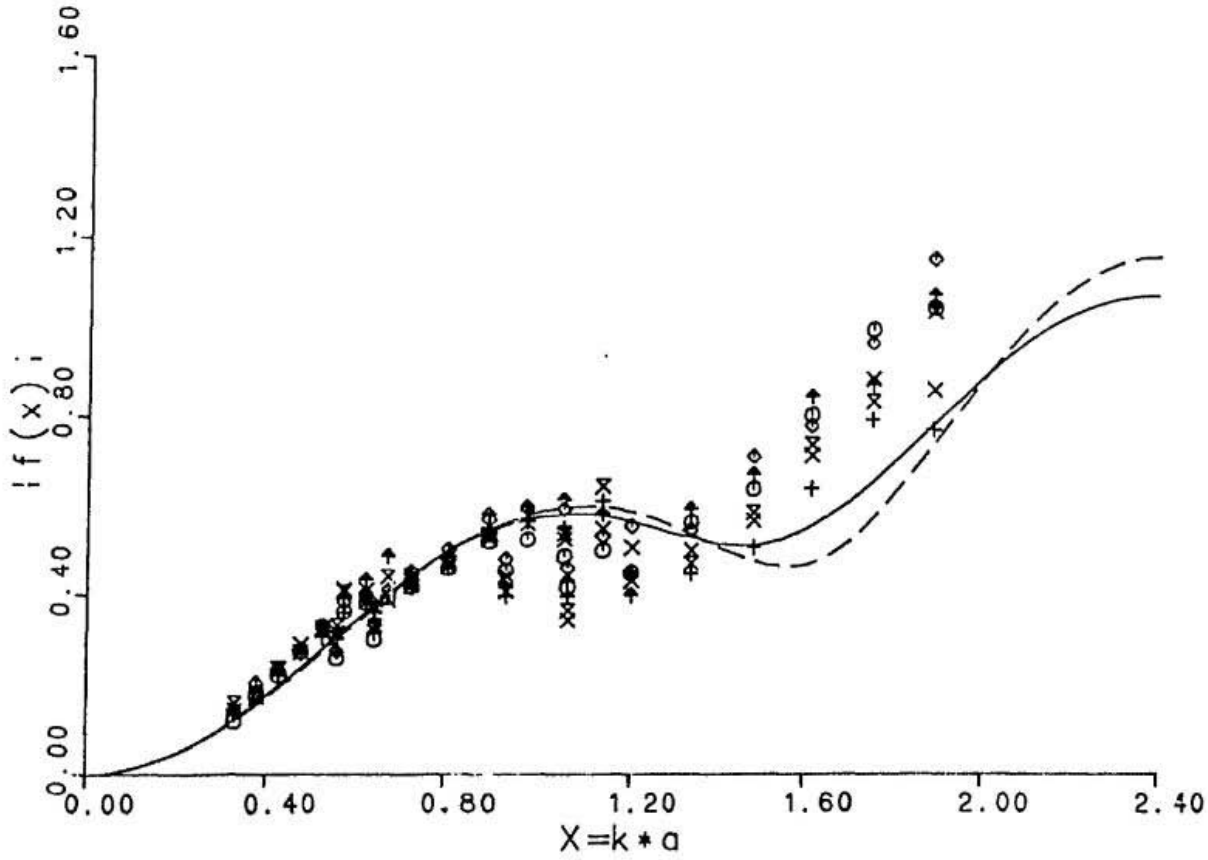

Figure 5.8: Backscatter form function $| f_\infty(x) |$ for beach sand plotted with the data in Figure 5.5, 5.6, 5.7

corresponding to 3 different particle sizes in Fig. 5.8. It is encouraging that the estimated values of $| f_\infty(x) |$ are substantially the same for the three sizes in the regions of overlap ($0.33 \leq x \leq 0.67$ for 115μm, and $0.56 \leq x \leq 1.1$ for 196μm, and $0.93 \leq x \leq 1.9$ for 327μm).

The measurement results show that agreement with the theoretical curve is quite good and exhibit similar curvature in the interval $0.33 \leq x \leq 1.9$. At higher values of x, the measured form functions are larger than predicted

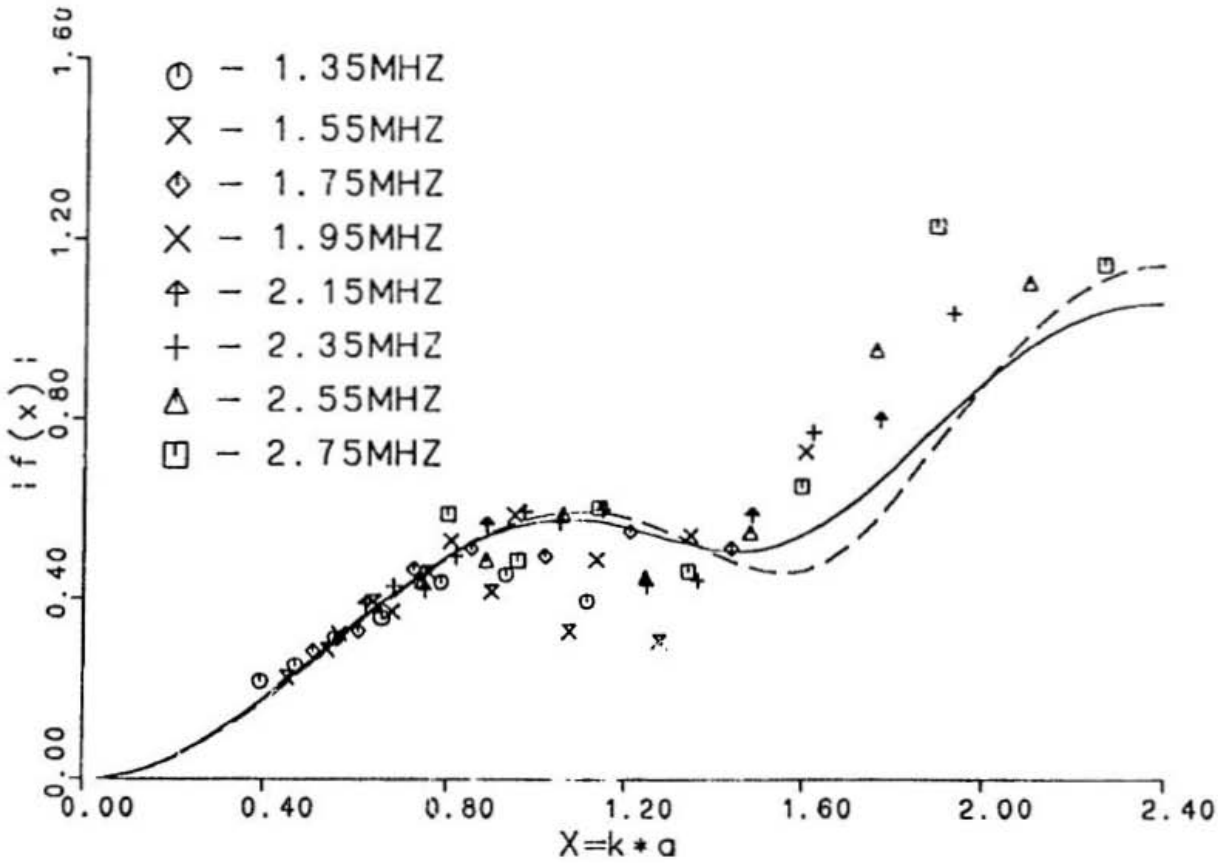

Figure 5.9: Backscatter form function $| f_\infty(x) |$ for beach sand measured for different size sand (see Table 5.5)

by the rigid movable spherical scatterer theory. This is similar to Hay's (1991) results, and could be due to particle shape irregularities since with increasing frequency, or decreasing ratio of wavelength to the size of particle, the particle shows relatively more irregularities. Therefore, the additional scatterering becomes larger.

Fig. 5.9 shows the results for the measured form factor when many different sand sizes, using a single concentration for each size, were measured.

T = 20.9 °C				C(m/s)=1484.4			
midpoint $2a_0(\mu m)$	137	165	196	231	275	327	390
concentration(g/l)	1.058	1.083	1.081	0.883	0.936	0.728	0.999

Table 5.5: T - temperature, C - acoustic speed in the water

The sizes and concentrations are listed in Table 5.5. It can be seen that the measured values follow the theoretical curve well and are similar to the measured data in Fig. 5.8. This indicates from another perpective that the average overall constant $\overline{B}$ we obtained by measuring sand of known size and concentration is reasonably good, and the relation shown in equation (4.19) is suitable for expressing the backscattering problem of suspended sand measured in the near field by a broadband transducer.

Chapter 6

CONCLUSIONS

In order to investigate the characteristics of the acoustical pressure in the transducer nearfield, a closed form expression for calculating the acoustical field transmitted by a circular piston with non-uniform surface velocity was derived. Using this expression to calculate the nearfield has the advantages of including neither approximations nor numerical integrations. The results show that the wave pattern produced by a 2.54 cm diameter circular piston having a frequency of 2 MHz and a uniform surface velocity is more complex and irregular than that of the same piston assuming the simply supporting boundary condition. This indicates that the surface velocity distribution plays an important role in the acoustical pressure of the nearfield

as mentioned in Hutchins et al. (1986). The average acoustical pressure on the receiver surface was calculated and shows little change with distance along the acoustical axis (less than 10%) which is similar to Hasegawa et al.'s results (1984). However it decreases with increasing distance. Thus, considering the beamwidth in the nearfield to be constant, for some applications, may be an oversimplification of the problem.

Experiments were carried out in a small tank to compare the theory with actual measurements, and to determine the overall system sensitivity as a function of frequency by self-reciprocity. The measurements show that the change of the average acoustical pressure on the receiver surface with distance, generated by a broadband transducer, is similar to theoretical calculation for a transducer with uniform vibration surface, instead of with nonuniform vibration surface (simply supported edge case) because of the effects of multi-vibration modes on transducer surface for a pulse excited transducer. The agreement of the overall system constants between measurements and calculations is reasonably good, especially at lower frequencies.

The relationship between the backscattered signal from suspended sediment and the size and concentration of sediment measured using a broadband

transducer in the nearfield is derived to be

$$V_0(\omega) = B(r,\omega)\sqrt{\frac{M}{x}} \mid f_\infty(x) \mid . \qquad (6.1)$$

It shows that square of output voltage is linearly proportional to mass concentration of sediment if multiple scattering is negligible. This relationship has been verified by experiments. Several experiments for measuring the form function, $\mid f_\infty(ka_0) \mid$, were carried out in the big tank with a turbulent jet circulation system. Although fluctuations occur in the backscatter signals, after averaging 200 times the results are shown to be stable and repeatable. The form factor measured by our system, within the range $0.32 \leq x \leq 1.9$, for different size or concentration follows the smoothed theoretical curve for a movable rigid sphere model reasonably well except for large x. The latter problem could be due to the irregular shape of the particles. By comparing the form function measured in the far field (Hay, 1991) using the same circulation system and different narrowband transducers, the two measured results are similar.

The results given in this thesis are promising. They indicate that it is feasible to determine acoustical scattering cross sections using broadband pulses and turbulent suspensions. The results presented here also indicate

the possibility of using broadband acoustical system for particle size and concentration measurements in the field.

References

Aldridge, E. E., The estimation of grain size in metal, in non-destructive testing, edited by X. Egerton, Harwell Post-Graduate Series (Oxford U. P., Oxford, 1969), pp. 31-45.

Arfken, G., Mathematical methods for physicists(Academic Press, New York and London, 1970), pp. 815.

Beecham, D., Ultrasonic scatter in metals: its properties and its application to grain size determination. Ultrasonics 4. 67-76 (1966)

Bateman, H., The Math. Analysis of Electrical and Optical Wave Motion On the Basis of Maxwell Equation (Cambridge University Press,New York,1914), pp. 160.

Cavanagh, E. and B. D. Cook.Gaussian-Laguerre description of ultrasonic field Numerical example:circular piston. J. Acoust. Soc. Am. 67, 1136-1140 (1980).

Clay, C. S. and H. Medwin, Acoustical Oceanography, John Wiley, New York, 1977, pp. 154-155.

Davis, M.C., Coal slurry diagnostics by ultrasound transmission, J. Acoust. Soc. Am. 64(2), 406-411 (1978).

Dekker, D. L., R. L. Piziali and E. Dong. Jr. ,Effect of boundary conditions on the ultrasonic-beam characteristics of circular disks, J. Acoust. Soc. Am. 56, 87-93 (1974).

Dietz, R. S., Deep scattering layer in the Pacific and Antarctic oceans, J. Mar. Res., 7. 430-442, (1948).

Dragonette, L. R., Richard H. V., Lawrence F., and Werner G. N., Acoustic reflection from elastic spheres and rigid spheres and spheriods. II Transient analysis. J. Acoust. Soc. Am., Vol. 55, 1130-1137 (1974).

Faran, Jr., J. J., Sound scattering by solid cylinders and spheres. J. Acoust. Soc. Am. 23, 405-418 (1951).

Fay, B., Theoretical consideration of ultrasonic backscatterering, Acoustica 28, 354-357 (1973).

Fisher, F. H. and V. P. Simmons, Sound absorption in sea water, J. Acoust. Soc. Am., 63, 558-564, (1977).

Flammer, G. H.,Ultrasonic Measurement of Suspended Sediment, U.S. Geologocal Survey Bulletin 1141-A, pp. 49 (1962).

Gaunaurd, G. and A. Kalnins, Resonances in the sonar cross-sections of (coated) spherical shells, Int. J. Solids Structures 18, 1083-1102 (1982)

Goebbel, K., S. Hirsekon, and H. Willems, The use of ultrasound in the determination of microstructure," IEEE Ultrason 45. Proc., 841-846 (1984).

Greenlaw, C. F. and R. K. Johnson, Physical and acoustical properties of zooplankton, J. Acoust. Soc. Am. 72, 1706-1710 (1982).

Greenspan, M., Piston radiator:some extensions of the theory.J. Acoust. Soc. Am. 65(3), 608-621 (1979).

Guyomar, D. and J. Powers.Boundary effects on transient radiation fields from vibrating, J. Acoust. Soc. Am. 77, 907-915 (1985).

Hanes, D. M., C. E. Vincent, D. A. Huntley and T. L. Clarke, Acoustic measurement of suspended sand concentration in the C^2S^2 experiment at stanhope lane, Prince Edward Island, Marine Geology, 81, 185-196, (1988).

Harris, G.R., Review of transient field theory for a baffled planar piston, J. Acoust. Soc. Am. 70(1), 10-20 (1981).

Hasegawa, T., N. Inove, and K. Matsuzawa, A new rigorous expansion for the velocity potential of a circular piston Source, J. Acoust. Soc. Am. 74, 1044-1047 (1983).

Hasegawa, T., N. Inove, and K. Matsuzawa, Fresnel diffraction: Some extensions of the theory, J. Acoust. Soc. Am. 75, 1048-1051 (1984).

Hay, A. E., On the remote acoustic detection of suspended sediment at long wavelengths, J. Geophys. Res., 88(c12), 7525-7542 (1983).

Hay, A. E., L. Huang, E. B. Colbourne, J. Sheng and A. J. Bowen, A high speed multi-channel data acquisition system for acoustic sediment transport studies, Proc. Oceans '88. 413-418 (1988).

Hay, A. E. and D. G. Mercer, On the theory of sound scattering and viscous absorption in aqueous suspensions at medium and short wavelengths, J. Acoust. Soc. Am. 78(5), 1761-1771 (1985).

Hay, A. E., Sound scattering from a particle-laden, turbulent jet. J. Acoust. Soc. Am., 90(4), 2055-2074 (1991).

Hess, F.R. and M.H. Orr, A wide range sonar system for oceanic investigations, Proc. Oceans'79, 79:27-32 (1979).

Hess, F.R. and K.W. Bedford, Acoustic backscatter system(ABSS):the instrument and some preliminary results, Marine Geology, 66. 357-379 (1985).

Hickling, R., Analysis of echoes from a solid elastic sphere in water, J. Acoust. Soc. Am.,34, 1582-1592 (1962).

Holliday, D. V., Acoustic Determination of suspended particles size spectra, Coastal Sediments '87 260-271, (1987).

Hutchins, D. A., H. D. Mair, P. A. Puhach and A. J. Osei. Continuous-wave pressure fields of ultrasonic transducers, J. Acoust. Soc. Am. 80(1), 1-12 (1986).

Jansen, R.H.J., The in-situ measurement of Sediment Transport by Means of Ultrasound Scattering. A Paper Presented at the Autumn meeting 1977 of the Dutch Acoustical Society. Utrecht, Nov. 9 (1977).

Jansen, R.H.J., An ultrasonic doppler scatterometer for measuring suspended sand transport. Ultrasonic International 79, Conference Proceedings, Graz, Austria, UI 79. 366-369 (1979).

Jansen, R.H.J., Combined scattering and attenuation of ultrasound as tool for measuring suspended sand transport, IAHR Workshop on Particle Motion and Sediment Transport, Rapperswil, Switzerland, April 6-8, p30, 1-30. 3.

Johnson, R. K., Sound scattering from a fluid sphere revisited, J. Acoust. Soc. Am. 61, 375-377 (1977).

Kikuchi, Y., Ed., Ultrasonic Transducers (Corona Ltd., Tokyo, 1969), pp. 336-346.

King, L.V., On the acoustic radiation field of the piezo-electric oscillator and the effect of viscosity on transmission, Can. J. Research XI 484-488 (1934).

Laura, P. A., Directional charateristics of vibrating circular plates and membranes, J. Acoust. Soc. Am. 40 1031-1033 (1966)

Lockwood , J. C. and J.G.Willette, High-speed method for computing the exact Solution for the pressure variations in the nearfield of a baffled piston, J. Acoust. Soc Am. 53, 735-741 (1973).

Love, R. H., Target strength of an individual fish at any aspect, J. Acoust. Soc. Am. 34,1582-1592 (1977).

Lynch, J. F., Theoretical analysis of ABSS data for HEBBLE., Mar. Geol., 66: 277-289 (1985).

Lynch, J. F., T. F. Gross, B. H. Brumley and R. A. Filyo, Sediment concentration profiling in HEBBLE using a 1-MHz acoustic backscatter system. Marine Geology, 99, 361-385, (1991).

Lynch, J. F. and Y. C. Agrawal, A model-dependent method for inverting vertical profiles of scattering to obtain particle size spectra in boundary layers, Marine Geology, 99, 387-401 (1991).

Ma, Y., V. V.Varadan, Acoustic response of sedimentary particles in the near field of high-frequency transducers. J. Acoust. Soc. Am. 34,3-10 (1987).

Marshall, J. S. and W. Hitschfield, Interpretation of the fluctuating echo from randomly distruted scatterers, Part I, Can J. Physics 31,962-994 (1953).

Numrich, S. K., V. V. Varadan, and V. K. Varadan, Scattering of acoustic waves by a finite elastic cylinder immersed in water, J. Acoust. Soc. Am. 70, 1407-1411 (1981).

Orr, H. H. and F. R. Hess, Remote acoustic monitoring of natural suspensate distributions, active suspensate resuspension, and slope/shelp Water Intrusions, J.Geophs. Res., 6145-6154. (1983).

Otnes, R. K. and L. Enochson, Digital Time Series Analysis, John Wiley & Sons, Inc., pp.467, (1972).

Press, W. H., B. P. Flannery, S. A. Teukolsky and W. T. Vetterling, Numerical Recipes, Cambridge, New York, pp. 818 (1986).

Peterson, B. A., V. V. Varadan, and V. K. Varadan, Scattering of acoustic waves by elastic and viscoelastic obstacles immersed in a fliud, Wave motion 2, 23-38 (1980).

Rayleigh, L., The Theory of Sound(Macmillan and Company, New York.1945), pp. 504.

Reid, J. M., Self-reciprocity calibration of echo-ranging transducers. J. Acoust. Soc. Am., 55, 862-868, April (1974).

Schaafsma, A.S. and D. Kinderen, W.J.G.J., Ultrasonic instrument for the continuous measurement of suspended sand transport, Proc. IAHR Symp. on Measuring Techniques in Hydraulic Research, Delft(Balkema Publ. Rotterdam, 125-136 (1985).

Schaafsma , A. S., Development of Silt Measuring Methods: Study of the Feasibility of Concentration Measurement with Ultrasound: Results, Report on Investigation F37/M2032 Part II, Delft Hydraulics, November (1988).

Seki, H., A. Granato, and R. Truell. diffraction effects in the ultrasonic field of a piston source and their importance in the accurate measurement of attenuation. J. Acoust. Soc. Am. 28, 230-238 (1954).

Shaw, E. A. G., On the resonant vibration of thick barium titanate disks, J. Acoust. Soc. Am., 28, 38-50 (1956).

Shaw, E. A. G. and R. J. Sujir, Vibration patterns of loaded barium titanate and quartz discs, J. Acoust. Soc. Am., 32, 1463-1467 (1960).

Sheng, J., and A.E. Hay, An examination of the spherical scatterer approximation in aqueous suspension of sand. J. Acoust. Soc. Am. 83(2), 598-610 (1988).

Sheng, J., Remote determination of suspended sediment size and concentration by multifrequecy acoustic backscatter, Ph. D. thesis, Department of Physics, Memorial University, St. John's, NF, Canada, (1990).

Sheng, J. and A. Hay, Vertical profiles of suspended sand concentration and size from multifrequency acoustic backscatter, submited to J. Acoust. Soc. Amer. (1991).

Siegelmann, R. A. and J. M. Reid. Analysis and measurement of ultrasound backscattering from an ensemble of scatterers excited by sine-wave bursts. J. Acoust. Soc. Am. 53(5). 1351-1355 (1973).

Thorne, P. D., C. E. Vincent, P. J. Hardcastle, S. Rehman and N. Pearson. Measuring suspended sediment concentrations using acoustic backscatter sevices, Marine Geology. 98, 7-16 (1991).

Timoshenko, S. and D. H. Young, Vibration Problems in Engineering, Third Edition, D. Van Nostrand Company, Inc. pp. 465 (1955).

Varadan, V. K., Y. Ma. and V. A. Varadan, A multiple scattering theory for elastic wave propagation in discrete random media, J. Acoust. Soc. Am., 77, 375-385 (1985).

Vincent, C. E. and M. O. Green, Field measurements of the suspended sand concentration profiles and fluxes and of the resuspension coefficient γ_0 over a rippled bed, J. Geophsical research, Vol. 95. 11591-11601, (1990).

Werby, M. and G. Gaunaurd, Classification of resonance in the scattering from submerged spheroidal shells insonified at arbitrary angles of incidence, J. Acoust. Soc. Am., 82, 1369-1377 (1987).

Williams, A.O., The piston source at high frequencies, J. Acoust. Soc. Am., 23, 1-6 (1951).

Young, R.A., J. Merrill, J.R. Proni, and T.L. Clarke, Acoustic profiling of suspended sediment in the marine boundary layer, Geophys. Res. Letters, 9(3), 175-178 (1982).

Zemanek, J., Beam behavior within the nearfield of a vibrating piston, J. Acoust. Soc. Am., 49, 181-191 (1971).

APPENDIX A

In order to show how the first several successive $B_n(Z)$ may be obtained, here we give the detail associated with calculating $B_2(Z)$ and $B_4(Z)$. The following three relations will be used in the calculation.

$$zh_n^{(2)}(z) = (2n-1)h_{n-1}^{(2)}(z) - zh_{n-2}^{(2)}(z) \qquad (A1)$$

$$(n+1)P_{n+1}(z) - (2n+1)zP_n(z) + nP_{n-1}(z) = 0 \qquad (A2)$$

$$\int z^{1-n}h_n^{(2)}(z)dz = -z^{1-n}h_{n-1}^{(2)}(z) \qquad (A3)$$

Then from Hasegawa, et al. (1983) we have

$$A_2(Z) = \int Zh_2^{(2)}(Z)P_2(\frac{Z_0}{Z})dZ$$

$$= -ZP_2(\frac{Z_0}{Z})h_1^{(2)}(Z) + h_0^{(2)}(Z)$$

and

$$A_4(Z) = \int Zh_4^{(2)}(Z)P_4(\frac{Z_0}{Z})dZ$$

$$= -ZP_4(\frac{Z_0}{Z})h_3^{(2)}(Z) + 5P_2(\frac{Z_0}{Z})h_2^{(2)}(Z) - h_0^{(2)}(Z)$$

So,

$$B_2(Z) = \int Z^2[Zh_2^{(2)}(Z)P_2(\frac{Z_0}{Z}]dZ$$

$$= Z^2A_2(Z) - 2\int Z[-Zh_1^{(2)}(Z)P_2(\frac{Z_0}{Z}) + h_0^{(2)}(Z)]dZ$$

$$= Z^2A_2(Z) - 2\int Zh_0^{(2)}(Z)P_0(\frac{Z_0}{Z})dZ + 2\int Z^2h_1^{(2)}[\frac{3Z_0}{2Z}P_1(\frac{Z_0}{Z}) - \frac{1}{2}P_0(\frac{Z_0}{Z})]dZ$$

$$= Z^2 A_2(Z) - 2A_0(Z) + 3\int Z Z_0 h_1^{(2)}(Z) P_1(\frac{Z_0}{Z})dZ - \int Z^2 h_1^{(2)}(Z) P_0(\frac{Z_0}{Z})dZ$$

$$= Z^2 A_2(Z) - 2A_0(Z) + 3Z_0 A_1(Z) + Z^2 h_0^{(2)}(Z) - 2A_0(Z)$$

$$= Z^2 A_2(Z) + 3Z_0 A_1(Z) - 4A_0(Z) + Z^2 h_0^{(2)}(Z)$$

Similarly, for $B_4(Z)$

$$B_4(Z) = \int Z^2[(Z h_4^{(2)}(Z) P_4(\frac{Z_0}{Z})]dZ$$

$$= Z^2 A_4 - 2\int Z[-Z P_3(\frac{Z_0}{Z}) h_3^{(2)}(Z) + 5P_2(\frac{Z_0}{Z}) h_2^{(2)}(Z) - h_0^{(2)}(Z)]dZ$$

$$= Z^2 A_4(Z) - 10A_2(Z) + 2A_0(Z) + 2\int Z^2 P_3(\frac{Z_0}{Z}) h_3^{(2)}(Z)dZ$$

$$= Z^2 A_4(Z) - 10A_2(Z) + 2A_0(Z) + 2\int Z^2 h_3^{(2)}(Z)[\frac{7Z_0}{4Z} P_3(\frac{Z_0}{Z}) - \frac{3}{4} P_2(\frac{Z_0}{Z})]dZ$$

$$= Z^2 A_4(Z) - 10A_2(Z) + 2A_0(Z) + \frac{7}{2} Z_0 A_3(Z)$$

$$-\frac{3}{2}\int Z P_2(\frac{Z_0}{Z})[5h_2^{(2)}(Z) - Z h_1^{(2)}(Z)]dZ$$

$$= Z^2 A_4(Z) - 10A_2(Z) + 2A_0(Z) + \frac{7}{2} Z_0 A_3(Z) - \frac{15}{2} A_2(Z)$$

$$+\frac{3}{2}\int Z^2 h_1^{(2)}(Z) P_2(\frac{Z_0}{Z})dZ$$

We know

$$B_2(Z) = Z^2 A_2(Z) - 2A_0 + 2\int Z^2 h_1^{(2)}(Z) P_2(\frac{Z_0}{Z})dZ$$

Therefore,

$$B_4(Z) = Z^2 A_4(Z) - 10A_2(Z) + 2A_0(Z) + \frac{7}{2} Z_0 A_3(Z) - \frac{15}{2} A_2(Z)$$

$$+\frac{3}{4}B_2(Z) - \frac{3}{4}[Z^2A_2(Z) - 2A_0(Z)]$$

$$= Z^2[A_1(Z) - \frac{3}{4}A_2(Z)] - [10A_2(Z) - 2A_0(Z)] + \frac{3}{2}A_0(Z)$$

$$+\frac{7}{2}Z_0A_3(Z) - \frac{15}{2}A_2(Z) + \frac{3}{4}B_2(Z)$$

Other $B_n(Z)$ may be obtained in a similar way.

APPENDIX B

Here, we rewrite equation(2.45)

$$B_n(Z) = Z^2[A_n(Z) - \frac{(n-1)}{n}A_{n-2}(Z)] + \frac{2(2n-1)}{n}Z_0A_{n-1}(Z) -$$
$$\frac{2(n-1)(2n-3)}{n}A_{n-2}(Z) - 2g_n(Z) + \frac{2(n-1)}{n}g_{n-2}(Z)$$
$$+\frac{n-1}{n}B_{n-2}(Z) \quad n>3\,. \quad (B1)$$

Differentiation of the two sides of equation (B1) and using equation(2.28) gives

$$Z^3h_n^{(2)}(Z)P_n(\frac{Z_0}{Z}) = 2Z[A_n(Z) - \frac{n-1}{n}A_{n-2}(Z)] + Z^3h_n^{(2)}(Z)P_n(\frac{Z_0}{Z})$$
$$-\frac{(n-1)}{n}Z^3h_{n-2}^{(2)}(Z)P_{n-2}(\frac{Z_0}{Z}) + \frac{2(2n-1)}{n}Z_0Zh_{n-1}^{(2)}(Z)P_{n-1}(\frac{Z_0}{Z})$$
$$-\frac{2(n-1)(2n-3)}{n}Zh_{n-2}^{(2)}(Z)P_{n-2}(\frac{Z_0}{Z}) - 2\frac{d}{dZ}g_n(Z)$$
$$+\frac{2(n-1)}{n}\frac{d}{dZ}g_{n-2}(Z) + \frac{n-1}{n}Z^3h_{n-2}^{(2)}(Z)P_{n-2}(\frac{Z_0}{Z})\,.$$

Rearranging above equation and using the relation

$$g_n(Z) + g_{n-2}(Z) = (2n-3)A_{n-2}(Z)\,,$$

we obtain

$$2ZA_n(Z) - \frac{2(n-1)}{n}ZA_{n-2}(Z) + \frac{2(2n-1)}{n}Z_0Zh_{n-1}^{(2)}(Z)P_{n-1}(\frac{Z_0}{Z})$$

$$-\frac{2(2n-1)(2n-3)}{n}Zh^{(2)}_{n-2}(Z)P_{n-2}(\frac{Z_0}{Z})+\frac{2(2n-1)}{n}\frac{d}{dZ}g_{n-2}(Z)=0. \quad (B2)$$

From the relations (2.17) and (2.18) for A_n the first two terms in (B2) become

$$2ZA_n(Z)-\frac{2(n-1)}{n}ZA_{n-2}(Z)$$

$$=-2Z^2h^{(2)}_{n-1}(Z)P_n(\frac{Z_0}{Z})+2Z^2h^{(2)}_{n-1}(Z)P_{n-2}(\frac{Z_0}{Z})-\frac{2(2n-1)}{n}ZA_{n-2}(Z)$$

$$=-2Z^2h^{(2)}_{n-1}(Z)P_n(\frac{Z_0}{Z})+2Z^2h^{(2)}_{n-1}(Z)P_{n-2}(\frac{Z_0}{Z})+\frac{2(2n-1)}{n}Z^2h^{(2)}_{n-3}(Z)P_{n-2}(\frac{Z_0}{Z})$$

$$-\frac{2(2n-1)}{n}Z\sum_{m=1}^{[\frac{n}{2}-1]}(-1)^{m+1}(2n-4m-3)h^{(2)}_{n-2m-2}(Z)P_{n-2m-2}(\frac{Z_0}{Z})$$

$$=-2Z^2h^{(2)}_{n-1}(Z)P_n(\frac{Z_0}{Z})+2Z^2h^{(2)}_{n-1}(Z)P_{n-2}(\frac{Z_0}{Z})$$

$$+\frac{2(2n-1)}{n}Z^2h^{(2)}_{n-3}(Z)P_{n-2}(\frac{Z_0}{Z})-\frac{2(2n-1)}{n}\frac{d}{dZ}g_{n-2}. \quad (B3)$$

Using relation

$$nP_n(Z')=(2n-1)Z'P_{n-1}(Z')-(n-1)P_{n-2}(Z'),$$

the first term on the rhs of (B3) can be rewritten as

$$-2Z^2h^{(2)}_{n-1}(Z)P_n(\frac{Z_0}{Z})=-\frac{2(2n-1)}{n}ZZ_0h^{(2)}_{n-1}(Z)P_{n-1}(\frac{Z_0}{Z})$$

$$+\frac{2(n-1)}{n}Z^2h^{(2)}_{n-1}(Z)P_{n-2}(\frac{Z_0}{Z}). \quad (B4)$$

Also using the relation

$$Z'h^{(2)}_n(Z')=(2n-1)h^{(2)}_{n-1}(Z')-Z'h^{(2)}_{n-2}(Z'),$$

the third term in (B3) becomes

$$\frac{2(2n-1)}{n} Z^2 h^{(2)}_{n-3}(Z) P_{n-2}(\frac{Z_0}{Z})$$

$$= \frac{2(2n-1)(2n-3)}{n} Z h^{(2)}_{n-2}(Z) P_{n-2}(\frac{Z_0}{Z}) - \frac{2(2n-1)}{n} Z^2 h^{(2)}_{n-1}(Z) P_{n-2}(\frac{Z_0}{Z}). \quad (B5)$$

Substituting equations (B4) and (B5) into (B3), and the resulting equation into equation (B2), we find that all terms cancel each other proving equation(2.15).